AN MRI BASED METHOD FOR DETECTION OF MICROCALCIFICATIONS

IN THE HUMAN BREAST

By

Richard Amador Baheza

Dissertation

Submitted to the Faculty of the

Graduate School of Vanderbilt University

in partial fulfillment of the requirements

for the degree of

DOCTOR OF PHILOSOPHY

in Biomedical Engineering

August, 2013

Nashville, Tennessee

Approved:

Professor Thomas E. Yankeelov

Professor John C. Gore

Professor Mark D. Does

Professor E. Brian Welch

Professor Daniel Gochberg

This work is dedicated to my family:

Maria Angela, Nancy, Nadia, Marlene, and Alfred

ACKNOWLEDGMENTS

LIST OF FIGURES

LIST OF TABLES

TABLE OF CONTENTS

CHAPTER I

INTRODUCTION

As the presence of microcalcifications in breast tissue can be an early indicator of cancer, the ability to detect calcium deposits with magnetic resonance imaging (MRI) is potentially of great clinical value. Unfortunately, direct detection of calcium deposits with traditional magnitude MRI is challenging as they appear as hypo-intense regions and cannot definitively be identified as calcium. However, calcium and tissue water have different magnetic susceptibilities, which produce noticeable differences in MRI phase images. This dissertation proposes to implement a new method for detecting microcalcifications using their characteristic susceptibility effects in MR phase images. The overall goal is to implement a method for detecting calcium deposits within tissue and evaluate the conditions needed for the method to work in practice to ultimately provide insight on the clinical value of the method for detecting microcalcifications in breast MRI at high field (7T). Towards this end we have established the following three specific aims:

Specific Aim 1: In simulated MRI data, apply cross-correlation analysis to identify calcium deposits and evaluate the influences of various MR parameters on the method. A spherical calcium deposit surrounded by tissue water will induce a disturbance with the shape of a dipole when placed in a static magnetic field. This shape

can be observed in MR phase images as positive lobes parallel to the main magnetic field, in a right handed coordinate system, with twice the magnitude of the negative shifts. We hypothesize that a calcification, either spherical or non-spherical, also generates a dipole-like disturbance, a shape that is very distinct from those of other perturbations, so that an object with a similar phase signature is likely to be a calcium deposit, which can reliably be found with pattern recognition. In order to test this hypothesis, a pattern recognition method was implemented using cross-correlation with a library of templates to detect the phase signatures of spherical calcium deposits within homogeneous tissue in simulated MR phase images. In addition, this method was applied to simulated images with different signal to noise ratios (SNRs) and spatial resolution containing calcium deposits of different sizes, shapes, and locations in order to determine the influence of SNR, spatial resolution, partial volume effects, and the deposit size and shape on the method.

Specific Aim 2: In experimental data, validate the predictions of Aim 1 and test the cross-correlation method for detecting deposits in tissue-like phantoms. The cross-correlation method was applied to MR images of phantoms to validate the results found in simulations and to test the method for detecting deposits within tissue-like background. The method was applied to MR phase images of gel phantoms containing 1 mm spherical calcium-like deposits to determine the influences of SNR, spatial resolution, and partial volume effects. In order to determine the effects of deposit shape and size on the method, the method was applied to MR phase images of gel

phantoms containing calcium fragments with average length, width, and height between 0.2 mm and 0.8 mm. Unlike calcium fragments and calcium-like deposits immersed in a homogenous gel, actual calcium deposits within tissue are surrounded by other structures that can modify the phase signature of the dipole and, therefore, adversely affect detection. We hypothesize that cross-correlation analysis can robustly identify phase signatures of calcium deposits in the presence of background phase signatures common in a tissue-like phantom. In order to test this hypothesis, we applied the method to detect calcium-like deposits that had been inserted into chicken breast. Additionally, receiver operator characteristic (ROC) curve analysis was employed to determine the optimal cut-off value of the cross-correlation index that maximizes sensitivity and specificity.

Specific Aim 3: Apply cross-correlation to detect simulated microcalcifications in breast MR images of healthy controls to estimate the clinical value of the method. We hypothesize that optimized cross-correlation analysis can robustly identify simulated (realistic) calcium phase signatures present in clinical MRI exams. In order to test this hypothesis, we used microcalcifications obtained from biopsy samples of malignant breast cancer to generate realistic dipole fields, which were then inserted *in silico* into healthy control subject breast MR images (acquired with optimized MR parameters for detection). Cross-correlation analysis was then applied to these simulated data to detect the microcalcifications. ROC analysis was used to compare the sensitivity and specificity of this method with that of mammography.

CHAPTER II

BACKGROUND AND SIGNIFICANCE

Breast Cancer and Calcium Deposits

Detection of calcifications is critical in the diagnosis of breast cancer using X-ray mammography. In a mammogram, the presence of calcifications indicates regions where cancer may be present, and the morphology and distribution of the deposits are associated with the histology and malignancy of the cancer. In the Breast Imaging Reporting and Data System (BI-RADS) Atlas, the American College of Radiologists (ACR) recommends using calcification morphology, distribution, and number for determining malignancy (1). Table II-1 shows examples of X-ray images of benign and malignant microcalcifications divided by their BI-RADS category (2). In general, benign calcium deposits are macrocalcifications > 1 mm with smooth and dense shapes over a larger area, while malignant calcium deposits are microcalcifications that are either clustered or linear (Table II-1) (2). Clustered microcalcifications have at least 4-5 punctate or pleomorphic calcifications < 1 mm within a 1 cm^3 volume, and linear microcalcifications have thin irregular and discontinuous, linear or branching shapes with widths < 0.5 mm (Table II-1) (2).

While mammography is the gold standard for calcification detection and classification, it does have several limitations. In particular, precise spatial localization of deposits is difficult due to overlapping and relatively poor contrast between

anatomical structures observed in projection imaging. Furthermore, the effectiveness of mammography is limited in important sub-populations with an already high risk of developing cancer. The sensitivity of mammography decreases for women with dense fibroglandular breast tissue and, unfortunately, this is associated with a significantly higher risk of developing cancer (3). Mammography also exposes the breast to ionizing radiation capable of disrupting molecular DNA bonds. As women who carry mutations in either *BRCA1* and/or *BRCA2* breast cancer susceptibility genes have an impaired DNA repair mechanism, exposure to ionizing radiation can exacerbate DNA damage and, therefore, increase their risk of developing abnormal cell growth and cancer (4-5).
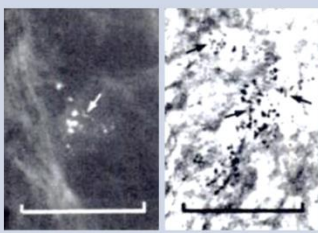
Table II-1 Classification of microcalcifications			
American College of Radiologists (ACR) **Breast Imaging Reporting and Data System (BI-RADS)**			
Microcalcification classification in categories 0-6			
Category	2: Benign	2: Benign	4-5: Suggestive of Malignancy
Size	> 1 mm	> 0.5 mm	< 1mm
Shape	Smooth & dense over large area	Thin linear & discontinuous	Clustered, pleomorphic, & punctate; 4-5 within 1 cm^3
X-ray Image scale=1cm			

Table modified from (1) and (2).

A magnetic resonance imaging (MRI) based technique for locating calcium deposits is a potentially advantageous alternative to mammography, specially for women with

dense fibroglandular tissue and/or *BRCA* mutations because it is not adversely affected by tissue density and does not use ionizing radiation. Additionally, MRI has 3D spatial localization capabilities and can be combined, in the same imaging session, with more established cancer imaging techniques such as dynamic contrast enhanced MRI (DCE-MRI) (6) and diffusion weighted MRI (DW-MRI) (7), to potentially offering a more reliable method to differentiate benign and malignant breast lesions.

Calcium Deposits in MRI

Calcium appears as a hypo-intense region in MR magnitude images. As iron and hemorrhage also appear hypo-intense, it is difficult to definitively identify calcium directly. Figure II-1 shows MRI and computed tomography (CT) of a images of a brain section containing a rare case of a calcified hemorrhage (8). T_2^* (panel a), T_1 (panel b), and T_2 (panel c) weighted images do not show the lesion; however, the CT image (panel d) reveals the presence of calcium as indicated by the arrow. as calcium is more diamagnetic than tissue water, the calcium deposits create local magnetic field distortions in the surrounding tissue. Since these magnetic field distortions can be detected by MRI, it is therefore possible to indirectly detect calcium deposits *via* susceptibility induced changes by MRI.

The (volume) magnetic susceptibilities of tissue water, calcifications, deoxygenatied whole blood, and iron are (in dimensionless SI units) -9×10^{-6}, -11×10^{-6}, -7.9×10^{-6}, and -11×10^{-1}, respectively. Thus, calcifications are more diamagnetic than tissue water while blood and iron are more paramagnetic than tissue water (9-10). These

6

susceptibility differences are noticeable in gradient echo phase images. Figure II-2

illustrates gradient echo images of micrometer-sized paramagnetic iron oxide particles

(MPIO) within a gel (11). The particles appear hypo-intense in magnitude images (panel

a), and their corresponding B_0 disturbances appear in the phase images (panel b). The

magnified view of these disturbances (panel c) indicates that the particle creates a

dipole shaped disturbance with the positive lobes parallel to B_0 and negative lobes

perpendicular to B_0. A 3D view of the dipole (panel d) reveals more details of the shape

of the lobes.
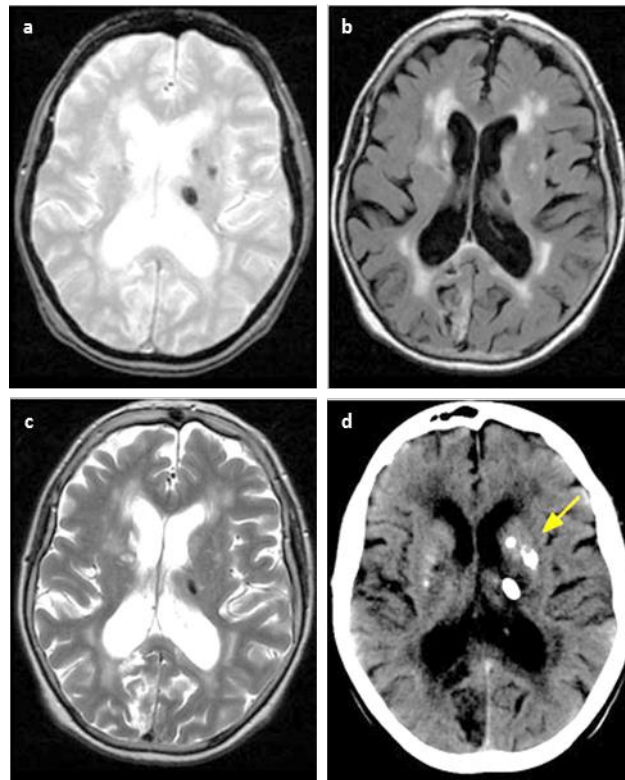
Figure II-1. Calcifications in MRI and CT. MRI of brain containing calcified hemorrhage lesion, T_2^* (a), T_1 (b), and T_2 (c) weighted images do not indicate the presence of calcium. The CT image (d), however, reveals calcium, indicated by the arrow (8).

The dipole shape φ_p is described mathematically by

$$\Delta\varphi_p(\mathbf{r},\theta) = \begin{cases} 0 & \text{for } r < a \\ \gamma TE \dfrac{\Delta\chi}{3}\dfrac{a^3}{r^3}(3\cos^2\theta - 1) & \text{for } r > a \end{cases} \qquad (\text{II-1})$$

where, χ_i and χ_w represent the volume magnetic susceptibility of iron and gel water, respectively; $\Delta\chi = (\chi_i - \chi_w)$; a is the radius of the spherical object; B_0 the magnitude of the static magnetic field; and r and ϑ are the usual polar coordinates (12). The polarity of the dipole depends on the susceptibility difference. In the case of calcium, the susceptibility difference is positive so that the polarity of a dipole generated by a calcium deposit will have the positive lobes parallel to $\mathbf{B_0}$, and the negative lobes perpendicular to $\mathbf{B_0}$.
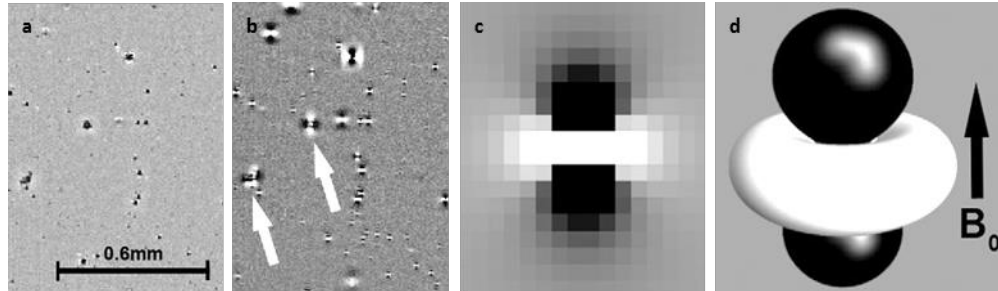
Figure II-2. MRI of MPIO within gel. The particles appear as hypo-intense regions in magnitude images (panel a) and as dipoles in the phase images (panel b); magnified view of the dipole (panel c) and 3D representation (panel d) provide more detail in the phase signature of the particle. (11).

To date, there have been a few reports on detecting calcium deposits in human brain and breast by exploiting the differential susceptibility effects of calcifications and glandular tissue on the MR signal (9, 13-15). We now briefly summarize the results of those studies.

The intracranial calcification was differentiated from hemorrhage in the gradient echo phase images on the basis of magnetic susceptibility differences (9). Intracerebral hematomas contains paramagnetic substances such as methemoglobins and ferritines while calcifications are mainly composed of calcium hydroxyapatite or apatite-like minerals that are more diamagnetic than brain tissue water. Therefore, hematomas and calcifications will act as dipoles with opposite orientations. The phase shift of a profile, perpendicular to B_0, along the line that passes through the center of the location of the dipole, will experience a phase shift with the same polarity of the lobes parallel to B_0; a negative shift in the case of paramagnetic dipoles and a positive shift in the case of diamagnetic dipoles. By studying the phase shifts in profiles along the location of suspicious lesions in brain, the authors were able to distinguish between hemorrhages and calcifications. Figure II-3 illustrates the identification of hemorrhages and calcifications in brain using the phase profile method (9). Panel a shows the MR phase image of a patient who had experienced a right putaminal hemorrhage containing suspicious lesions. Panel b indicates the profile along one of the lesions which indicates a paramagnetic type shift suggestive of a hemorrhage. Panel c shows the corresponding CT image which does not indicate the presence of calcium, consistent with a hemorrhage. Conversely, panel d shows the MR phase image of a patient with multi-infarct dementia containing suspicious lesions. Panel e displays the profile along one of the lesions that indicates a diamagnetic type shift indicating the presence of calcium. Panel f shows the corresponding CT image which verifies the presence of calcium (9).
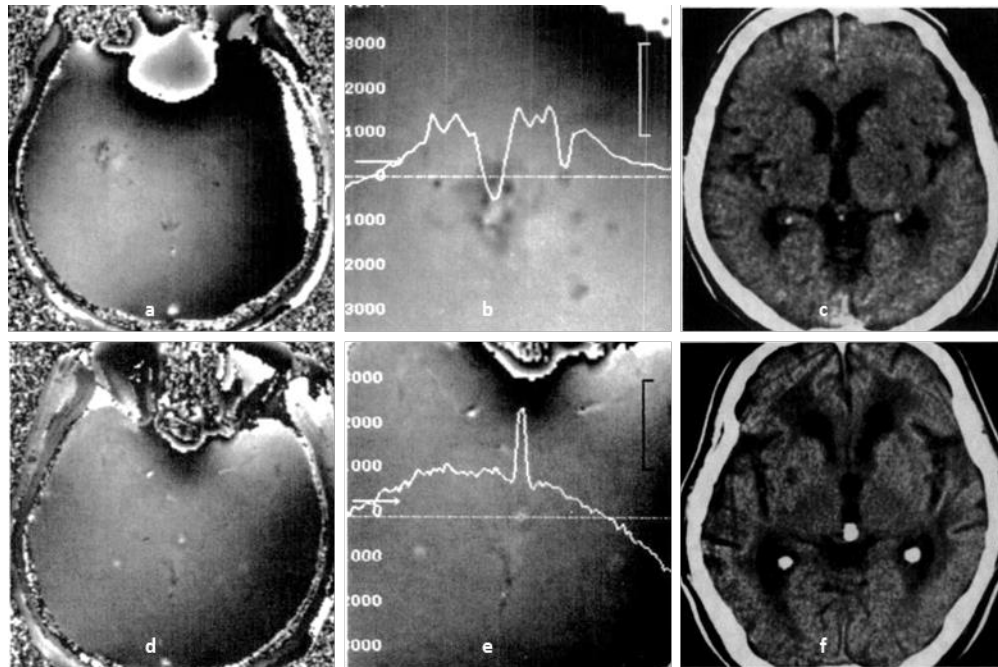
Figure III-3. Calcium and hemorrhage lesion detected *via* phase profile shift. Panels a and d show MR phase images of brain containing suspicious lesions, indicated by the arrows. Panels b and e depicts the phase profiles along the lesions indicating the paramagnetic (panel b) and diamagnetic (panel d) type shifts suggesting hemorrhage and calcium, respectively. Panels c and f illustrate the CT images in agreement with the nature of the lesion found using the profile shifts. (9).

A preliminary application of susceptibility weighted imaging (SWI), a technique used to generate images with susceptibility differences as the source of contrast (16), for detecting calcifications has been tested in breast phantoms and in breast cancer patients with mammographic confirmation of calcium deposits (13). The local magnetic field distortions induced by calcium deposits appear as positive phase shifts in 3D gradient echo MR images. SWI applies a series of phase filters to enhance these positive phase shifts and generates a mask. The mask is then applied to the magnitude images resulting in images with contrast due to differences in tissue magnetic susceptibilities . Figure II-4 shows an example of the detection of calcification in breast using SWI (13).

The SWI image (panel a) was obtained by overlaying the corrected phase image (panel b) in the magnitude image (not shown). The authors confirmed the presence of calcifications by X-ray mammography (panel c) (13).
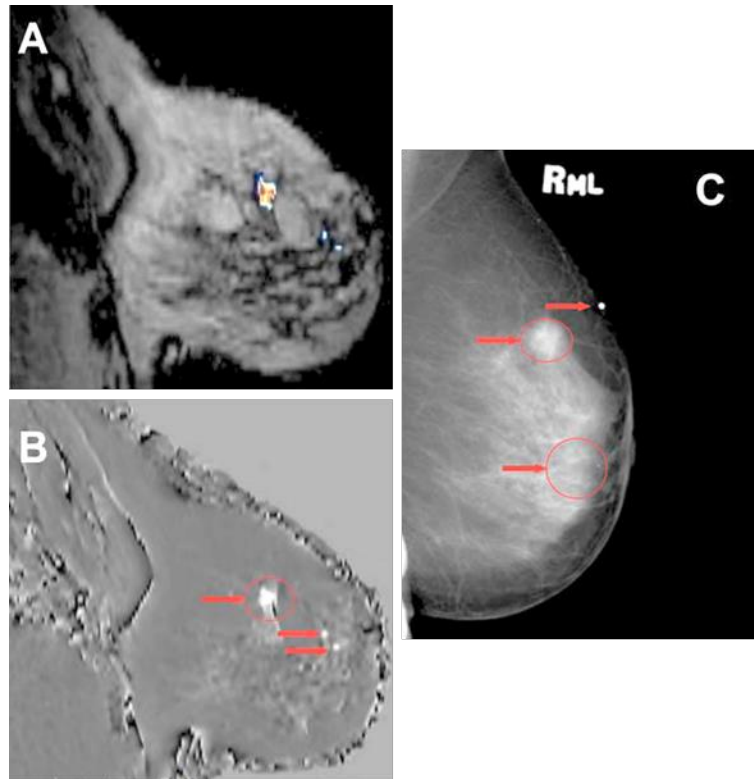
Figure III-4. Calcification detection using SWI. The SWI image (panel a) with corrected phase (panel b) overlayed indicate the presence of microcalcifications confirmed by X-ray mammography (panel c) (13).

However, this method uses a simplified version of the magnetic perturbations by considering them only as positive phase shifts (generated by calcium surrounded by tissue), or negative shifts (when created by iron or blood vessels surrounded by tissue). The actual perturbation induced by a calcium deposit has a dipole shape with positive phase shifts parallel to B_0, and negative phase shifts perpendicular to B_0 (12). Similarly, blood vessels will also produce both phase shifts—negative phase shifts parallel to B_0,

and positive phase shifts perpendicular to B_0. Therefore, contrast in a susceptibility weighted image will not only be from the calcium deposits, but also from other objects like blood vessels and iron. In addition, the size of the microcalcifications reported in SWI corrected phase images of the breast phantoms were 10-20% larger than the size of the same microcalcifications found in CT (0.4-1.5 mm) (13); therefore the method overestimated the true microcalcification size. Since deposit size is a key feature for classifying the associated cancer as malignant or benign (1), the use of this particular form of SWI for classifying microcalcifications may be limited.

In another attempt to identify calcium deposits in breast MRI, the directional blurring effect generated by the difference in the susceptibility of calcifications and glandular tissue was suggested as an indicator of the presence of calcium deposits (14). The blurring effect produced by clusters of spherical calcifications was simulated and implanted into 2D spin echo breast images from healthy volunteers and then statistical texture analysis was used to identify the blurring. The spatial gray level dependence method was used to detect localized blurring with sensitivity between 88.9 and 94.4% and specificity between 99.7 and 100%. Unfortunately, these results only showed that texture analysis works well for detecting blurring effects. Also, the sizes of the calcifications, simulated and detected, were not stated; therefore, the range of microcalcification sizes detectable with the method remains unknown. Additionally, as the method was not validated using actual MR images containing microcalcifications, the clinical value of the method for detecting calcium deposits in the human breast remains unknown.

Stehouwer et al tested the feasibility of detecting microcalcifications with high-field (≥3T) MRI by exploiting the effect of the difference in susceptibility of calcifications and glandular tissue on the phase signal in phantoms and in *ex vivo* breast tissue containing microcalcifications (15). The perturbation induced by a spherical calcium deposit has a dipole shape and the phase derivative of the distortion appears as a six-lobed shape (12). Since this pattern is very uncommon, it was used as an indicator of the presence of calcium deposits. Sub-millimeter calcium deposits were successfully detected in multi-echo fast field gradient echo 3D images in phantoms and in a breast tissue sample (17). However, clinical application of the method was not demonstrated. In addition, detection of the six-lobe pattern relies on visual inspection of the phase derivative and has no quantitative criteria for determining the presence and size of a deposit.

The above MRI based methods for detecting calcium deposits are good approaches but have thus far had limited clinical application. In this work, an alternative method is proposed: cross-correlation between the tissue under investigation and a template (the dipole shape associated with a calcification in breast tissue). In the following chapter, this method is described in detail and applied to simulated data containing microcalcifications with a relevant range of sizes associated with malignancy to determine the influence of various MR parameters on the method.

CHAPTER III

DETECTING CALCIUM DEPOSITS WITH CROSS-CORRELATION IN SIMULATIONS

Introduction

The phase signature of a calcium deposit has a distinct dipole shape that can potentially be detected using cross-correlation. Cross-correlation provides a measure of similarity between two objects; when the objects are identical, the cross-correlation index is one and when the objects have no similarity at all, the index is zero. In order to find a particular object within an image using this method, a similarity matrix between the image and a template, which is a realistic, high signal-to-noise replica of the desired object, is computed. The matrix is obtained by systematically computing the sliding dot product between the mean pixel value of the template and the mean pixel value of an object-sized image region. In the matrix, regions where the object are more likely to occur have index values close to one while regions where the object are less likely to occur have index values close to zero. In addition, the cross-correlation index can be used to study how the quality of the image affects the detection method. For instance, identical images containing the same deposit, but with different levels of noise, will result in different cross-correlation indices; the image with less noise will have a higher index.

The goals of the study presented in this chapter are to (a) use cross-correlation to locate calcium deposits between 0.2 and 1.0 mm in simulated data generated with

different MR parameters and SNR values and (b) use the cross-correlation index changes to determine the influences of these MR parameters on the method.

Methods

Simulated magnitude and phase images

To investigate how cross-correlation performs under different conditions, we applied cross-correlation to simulated MR images of calcium deposits surrounded by tissue under different conditions of noise, spatial resolution, and position within a voxel. All simulations employed Matlab version 7.10.0.499 (Mathworks, Natick, Massachusetts).

The calcifications were modeled as spherical objects immersed in homogeneous material. Figure III-1 shows the calcium model (panel a). Different diameters were considered to include the relevant range of calcification diameters measureable with X-ray mammography; important sizes to note are 0.25 mm, the smallest detectable deposit size (18); 0.35 mm, the size at which observers are able to correctly identify the shapes of deposits (19); ≤0.5 mm, the deposit size range associated with malignancy; and >0.5 mm, which are associated with benign tumors (2, 20). Thus, the diameters of the spheres in the simulations were set between 0.2 and 1.0 mm, with a step size of 0.1 mm.

Simulation of gradient echo 3D MR images at 7T were performed using discrete descriptions of spherical deposits surrounded by tissue water. The deposits and tissue

water were discretized using small cubical volumes called "element voxels". Figure II-1

illustrates the division of the calcium deposit into element voxels (panel b). The element

voxels contained a set of appropriate physical values, described below, necessary to

compute the gradient echo MR images. The size of each element voxels depended on

the size of the deposit. For deposit sizes between 0.2 and 1.0 mm (with a step size of 0.1

mm) element voxel sizes between $(6\ \mu m)^3$ and $(30\ \mu m)^3$, with 3 µm increments, were

used. The simulated images had larger image voxel sizes than the element voxels used

to discretize the deposit. The image voxel sizes were between 0.2 mm and 1.0 mm in

steps of 0.2 mm.
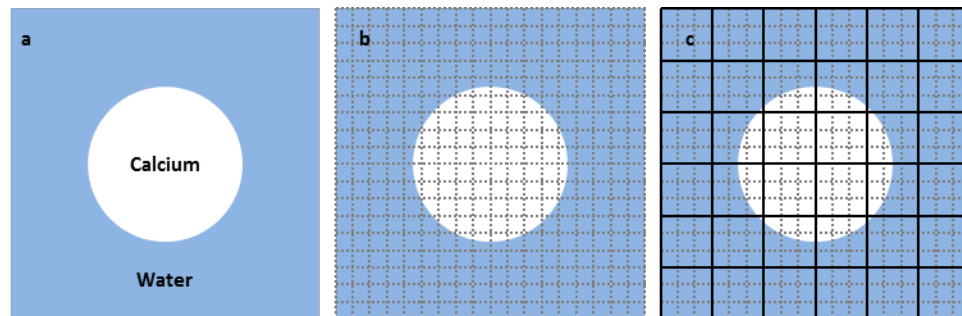
Figure III-1. Calcium deposit model. Calcium is modeled as a spherical object surrounded by water (panel a). The model is discretized using element voxels, indicated by the dashed lines, containing a set of appropriate physical values (panel b). After the complex image is computed, elements voxels are added to generate image voxels, indicated by solid lines (panel c).

Each element voxel was assigned to be calcium or tissue along with corresponding

physical values for proton density, ρ, the longitudinal and transverse relaxation time, T_1

and T_2, respectively, and the magnetic susceptibility, χ (the last three as appropriate for

7T). Element voxels within the spheres were set to the (volume) magnetic susceptibility

of -11×10^{-6} (SI dimensionless units), which is the susceptibility of calcium deposits (9);

and the element voxels within the tissue water were set to the susceptibility of tissue water -9×10^{-6} (SI dimensionless units). The density was set to 1×10^{6} arbitrary units (au) for water and 0 au for calcium. The element voxels within the tissue water were set to the relaxation time constants of glandular breast tissue water at 7T, T_1 and T_2 of 1622 ms and 64 ms, respectively (22). Since calcium density was set to zero, there was not magnitude or phase computed within the deposit. However, the susceptibility difference between calcium and water did created a phase disturbance surrounding the deposit.

Simulations of gradient echo 3D MR images of the deposits were divided into two separate parts: 1) the phase perturbation φ of the deposit, computed using the magnetic susceptibility distribution of the virtual deposit, and 2) magnitude, computed using T_1, T_2, ρ, and the field perturbation. We present each of these components separately in the next two sections.

Static field perturbation

There is a mature literature on methods for computing the perturbation of the field caused by the magnetic susceptibility of an object placed in a static magnetic field. Some are based on finite difference calculations (23-24) or integral methods (25), which work well for objects with irregular shapes, but are computationally expensive. A faster method uses the analytical solution for the perturbation field of objects with regular shapes such as cylinders or spheres (12). In our efforts, we used a spherical calcium deposit during the initial simulations in order to exploit the analytical solution. However,

in later experiments in which we studied more complicated geometries (see Chapter V),

we simulated the field perturbation of actual calcium deposits with irregular shapes, and

therefore selected a fast method that does not require *a priori* knowledge of the

distribution. Salomir *et al* (26) derived a transformation for computing the field

perturbation, $\Delta B_z(\mathbf{x}, \mathbf{y}, \mathbf{z})$, due to a particular susceptibility distribution, $\chi(\mathbf{x}, \mathbf{y}, \mathbf{z})$ that is

exposed to a static magnetic field, $\boldsymbol{B}_0$. In the Fourier domain,

$$\Delta \tilde{B}_z(\mathbf{k}) = B_0 \tilde{\chi}(\mathbf{k}) \cdot \left(\frac{1}{3} - \frac{k_z^2}{\mathbf{k}^2} \right) \tag{III-1}$$

where the overstrike "~" denotes a three-dimensional Fourier transform, k_z is the z-

component of the k-space vector parallel to the main magnetic field, and $\mathbf{k}^2 = k_x^2 + k_y^2 + k_z^2$

is the magnitude of the k-space vector. Using this transformation the field perturbation

can be computed without *a priori* knowledge of the distribution. Of note, the

computational time of calculating the field perturbation is not prohibitive as it only

requires the three-dimensional Fourier transform of the susceptibility distribution as

input.

Signal and image generation

The signal in each element voxel was computed using the signal intensity equation

for a standard gradient echo acquisition. The signal intensity and phase were computed

separately and then combined to form the complex signal. The signal intensity at

position *r* was computed using

$$S(r) = \rho_0 \cdot \frac{\left(1 - e^{-TR/T_1}\right) \cdot \sin(\alpha) \cdot e^{-TE/T_2^*}}{\left(1 - \cos(\alpha) \cdot e^{-TR/T_1}\right)} \quad , \tag{III-2}$$

where TR is the repetition time, α is the flip angle, T_1 is the longitudinal relaxation time, ρ_0 is the spin density in location r, T_2^* is the apparent transverse relaxation time. The phase, φ, was computed using

$$\varphi(r) = \gamma TE \Delta B(r) \quad , \tag{III-3}$$

where φ is the phase at position $\boldsymbol{r}$, γ the gyromagnetic ratio, TE is the echo time, and $\Delta B(r)$ is the deviation of the induced magnetic field at position $\boldsymbol{r}$. This equation uses the right handed coordinate system. The signal in each element, S_e, was computed using

$$S_e(r) = S(r)e^{i\varphi(r)} \quad . \tag{III-4}$$

In each image voxel, the signal S_I was computed as the vector sum of the complex signal of each element voxel within the image voxel using

$$S_I = \sum_1^n S_e(r_n)e^{i\varphi(r_n)} \quad , \tag{III-5}$$

where n is the number of element voxels in each image voxel. Figure III-1 illustrates the spatial relationship between element voxels and image voxels (panel c). The magnitude M and phase P in each image voxel where computed using $M = \sqrt{S_{IRe} + S_{IIm}}$ and $P = \tan^{-1}(S_{IRe} / S_{IIm})$, were S_{IRe} and S_{IIm} are the real and imaginary components of S_I, respectively.

To mimic experimental conditions, noise was generated and (independently) added to the real and imaginary components of the complex signal to yield SNR values with a range of [5,95] in steps of 10. Noise was generated using a normal random distribution

function with a mean of zero and a standard deviation of one. The SNR was calculated as the ratio of the mean value of the signal magnitude within a region of interest (ROI) to the standard deviation of the signal magnitude over the same region. The ROI was measured far from the calcium deposit, at the vertex of the image, to avoid areas with possible signal loss due to the field perturbation, ΔB, present at the boundaries of the deposit.

The phase range in the simulated phase images was constrained to [-π, π] (rad) by adjusting the *TE* to prevent phase wrapping. Phase images can contain a wide range of values depending on *TE*, orientation and magnitude of B_0, size of the spherical object, differences in magnetic susceptibilities, position of the spherical object within the voxel, and resolution of the image. Thus, some parameters need to be adjusted to contain the phase values within the desired range. The *TE*s needed to restrict the phase between -1, and 2 rad in the 3D gradient echo simulations of spherical deposits with diameters between 0.2 and 1.0 mm (in steps of 0.1 mm) and isotropic voxel sizes between 0.2 and 1.0 mm (in steps of 0.2 mm) at the main static field of 7T were computed and are summarized in Table III-1. The magnitude of the images for these *TE*s is also computed and is expressed as a percentage of the initial maximum signal when *TE*=0 (see Table III-1). For combinations with very long *TE*'s, the signal drops to zero and therefore the phase cannot be measured. Deposits in these combinations cannot be detected because their phase signature cannot be measured; these combinations are indicated by a "()" in Table III-1.

Table III-1. Gradient echo simulations computed to constrain phase within [-π, π]					
	TE (ms), signal intensity (%)				
Deposit size (mm)	Resolution (mm)				
	0.2	0.4	0.6	0.8	1
0.2	12.5, 82	(595, 0)	(3336, 0)	(5350, 0)	(11710, 0)
0.3	3.72, 94	17.4, 76	(595, 0)	(2371, 0)	(5750, 0)
0.4	1.9, 97	12.6, 82	91, 24	(584, 0)	(2070, 0)
0.5	1.3, 98	6.4, 91	29, 63	(177, 6)	(595, 0)
0.6	1.3, 98	3.7, 94	12.5, 82	17.3, 76	197, 4
0.7	1.5, 98	2.5, 96	7.7, 89	17.7, 83	82, 27
0.8	1.2, 98	1.9, 97	5.3, 92	12.6, 82	12.1, 83
0.9	1.0, 98	1.6, 98	3.8, 94	8.9, 87	11.8, 83
1	1.3, 98	1.3, 98	2.7, 96	6.4, 91	12.5, 82

"()" Indicates combinations where deposits cannot be detected because their phase signature cannot be measured

Identifying calcifications via cross-correlation method

In simulated and experimental phase images, the positions of calcium deposits and their sizes were determined using pattern recognition *via* cross-correlation. The cross-correlation coefficient matrix between a target image and an individual template was computed using Eq. (III-6):

$$C(i,j,k) = \frac{\sum_{l=1}^{p}\sum_{m=1}^{p}\sum_{n=1}^{p} T(l,m,n)A\left(i+l-\frac{p}{2},j+m-\frac{p}{2},k+n-\frac{p}{2}\right)}{\sqrt{\left[\sum_{l=1}^{p}\sum_{m=1}^{p}\sum_{n=1}^{p}T(l,m,n)^2\right]\left[\sum_{l=1}^{p}\sum_{m=1}^{p}\sum_{n=1}^{p}A\left(i+l-\frac{p}{2},j+m-\frac{p}{2},i+l-\frac{p}{2}\right)^2\right]}} \quad for \ \begin{cases} \frac{p}{2} < i < q-\frac{p}{2} \\ \frac{p}{2} < j < q-\frac{p}{2} \\ \frac{p}{2} < k < q-\frac{p}{2} \end{cases} \quad (III-6)$$

where $C(i,j,k)$ is the similarity matrix with dimensions $q \times q \times q$, A is the matrix containing the target image also with dimensions $q \times q \times q$, and T is the matrix containing the template with dimensions $p \times p \times p$. Matrices A and C are of the same size while T is

usually much smaller. The computed matrix contains cross-correlation coefficients with a range of [-1, 1]. The coefficient value indicates the degree of similitude between the template and target; a coefficient of 1 indicates a perfect match while a -1 indicates a target with the exact opposite value of the template. In principle, the location in the matrix where the cross-correlation has a maximum value (CCMV) will indicate the center position of the template in the image. Figure III-2 illustrates the process of pattern recognition *via* cross-correlation; cross-correlation between an image containing a circle (panel a) and a template containing the same circle (panel b) results in a cross-correlation matrix (panel c) where the presence of the circle is shown by the cluster of large cross-correlation indices and its exact location indicated by the CCMV.

Similarly, the positions of the calcium deposits and their sizes were determined using cross-correlation between simulated and experimental phase images and a library of templates containing the phase disturbances of calcium deposits with different sizes. The location of the CCMV in the matrix indicated the center position of the calcium signature in the phase images. The size of each deposit was determined by comparing the CCMVs obtained with the other templates in the library and was indicated by the maximum CCMV. The error in the size measurement depends on the deposit sizes used to generate the library. For example, when using a library of templates generated with sizes between 0.1 mm and 1.0 mm in steps of 0.1 mm, the 0.5 mm template can detect deposits between 0.45 and 0.55 mm; therefore, a deposit detected with this template will indicate sizes of 0.5 ±0.05 mm.
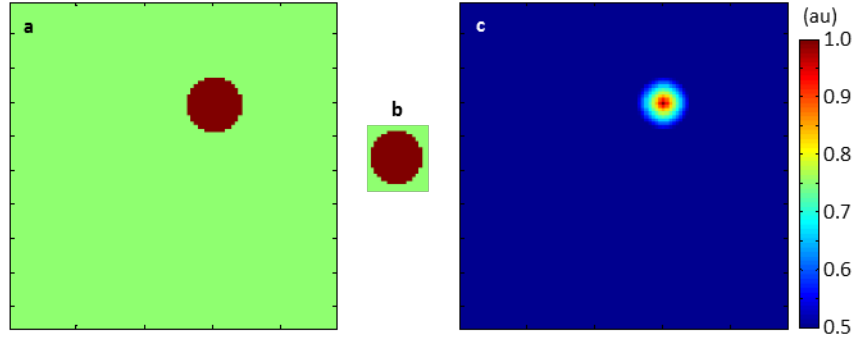
Figure III-2. Pattern recognition *via* cross-correlation. Cross-correlation between an image (panel a) and a template containing an specific pattern (panel b) will result in a cross-correlation matrix (panel c) where the presence of the pattern is indicated by a cluster of large cross-correlation indices and its exact location indicated by the maximum value (CCMV).

The templates in the library contain the phase signatures of spherical calcium deposits of different sizes surrounded by tissue. The template is generated using the aforementioned simulation method and the same parameters (i.e., object size, spatial resolution, *TE*, and B_0) used to acquire or simulate the target images.

The size of the template depends on the deposit size and was determined by studying the analytical expression for the induced magnetic dipole field generated by a calcium sphere surrounded by tissue water. The magnitude of the dipole ΔB_p is given by:

$$\Delta B_p(r,\theta) = \begin{cases} \dfrac{1}{3}\chi_w B_0 & \text{for } r < a \\ \dfrac{\Delta\chi}{3}\dfrac{a^3}{r^3}(3\cos^2\theta - 1) + \dfrac{1}{3}\chi_w B_0 & \text{for } r > a \end{cases} \tag{III-7}$$

where, χ_c and χ_w represents the volume magnetic susceptibility of calcium and tissue water, respectively; $\Delta\chi = (\chi_c - \chi_w)$; *a* is the radius of the spherical object; B_0 the magnitude of the static magnetic field; and r and θ are the usual polar coordinates (12). This equation indicates that the phase reaches the maximum magnitude when the radial

distance (**r**) equals the radius of the spherical object (*a*), and then the phase magnitude decreases as $1/r^3$. When **r** = 3*a*, the phase magnitude has lost 96% of its maximum value. We assume that using r ≤ 3*a* will include most of the characteristic phase changes therefore, we set the field of view (FOV) to three times the diameter of the sphere. A larger FOV will not include significant parts of the phase signature and will increase the template size and the computational time when computing the cross-correlation between the template and the target image.

The dimensions of the template matrix depend on the deposit size and spatial resolution; for example, a template for a 1 mm diameter deposit with a spatial resolution of $(0.2 \text{ mm})^3$ will have a FOV of 3×3×3 mm and a template matrix size of 15×15×15.

In order to determine if a template generated using a spherical deposit can be used to detect non-spherical deposits, cross-correlation was applied to simulated images of a spherical and non-spherical object. Also, high resolution phase signatures of the deposits were generated to study the differences between the phase signatures of the shapes. The shape of the non-spherical deposit was obtained from a calcium fragment in the CT experiments described in chapter IV, section *Computed Tomography*.

*Simulating the effect of **B**$_0$, spatial resolution, deposit size and shape,*

and location on cross-correlation

The influences of **B**$_0$, spatial resolution, SNR, and deposit location on the method were determined by studying the changes in CCMV obtained when detecting spherical

deposits of sizes between 0.2 and 1.0 mm (in steps of 0.1 mm) in images simulated with a magnetic field strength of 7T and isotropic voxel sizes between 0.2 and 1.0 mm (in steps of 0.2 mm), SNR between 5 and 95 (in steps of 10), and with different deposit locations. For each combination of deposit size, magnetic field strength, and voxel size, the individual and combined influences of SNR and deposit location on the method were determined as described below. The influence of SNR on cross-correlation was determined by studying changes on CCMV obtained when detecting the deposit in simulated MR images with SNR values between 5 and 95 in steps of 10. For each SNR value, 100 images were generated. Cross-correlation was applied to the images to locate the deposit and to determine the mean standard error of the measured CCMV.

The influence of deposit location on cross-correlation was determined by studying changes in CCMV obtained when detecting the deposit in different positions within the voxel. In simulated MR images with an SNR of 50, the deposit was systematically moved in the direction parallel to B_0 in 25 equally spaced locations from the center of the voxel to 2.5 times the voxel size. Only the location of the simulated deposit changed; the location of the deposit in the template remained the same (centered within a voxel). For each location of the deposit, 100 images were generated. Cross-correlation was applied to the images to locate the deposit and the mean CCMV and standard error were calculated.

Similarly, the influences of both SNR and the location of the deposit were determined by studying changes on CCMV obtained when detecting the deposit at different locations within a voxel and varying SNRs. Noise was added to the simulated

images to obtain SNR values between 5 and 95 in steps of 10. For each SNR value, the deposit was systematically moved within the voxel in ten equally spaced locations on each dimension, totaling 1000 different positions. Cross-correlation was applied to the images to locate the deposit and to determine the mean and standard error of the measured CCMV.

<div align="center">

Results

</div>

<div align="center">

Gradient echo magnitude and phase image simulations

</div>

Figure III-3 shows the simulated MR magnitude and phase images (SNR = 20) of a 1 mm spherical calcium deposit within a homogeneous background. In the magnitude image (panel a), there is a circular signal void created by the deposit; the phase image (panel b) shows the characteristic phase signature of the deposit: a dipole shape with the positive lobe parallel to the main magnetic field and twice the magnitude of the negative shifts perpendicular to the main magnetic field.
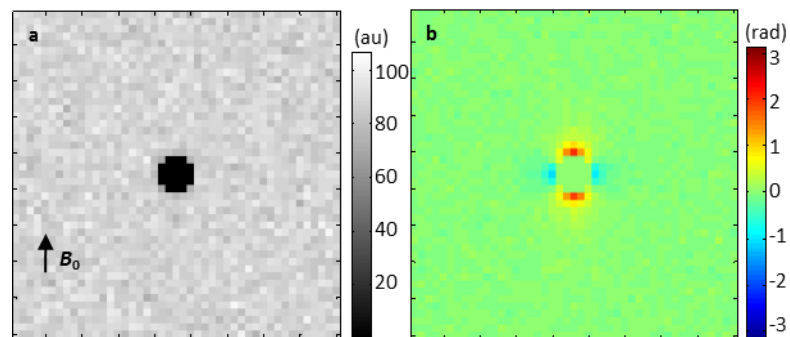
Figure III-3. MRI simulation of a 1 mm calcium deposit within tissue. The gradient echo magnitude image (panel a) shows a signal void created by calcium, and the phase image (panel b) depicts the characteristic phase signature of the deposit.

Identifying calcifications via cross-correlation

The cross-correlation method was applied to the simulated phase image in Figure III-3 to detect the deposit; the process is illustrated in Figure III-4. Cross-correlation between the template containing the phase signature of a 1 mm deposit (a) and a library of templates containing the phase signatures of calcium deposits with sizes between 0.2 and 2.0 mm (in steps of 0.2 mm). Panel b shows the templates of deposits with sizes 0.2, 1.0, and 2.0 mm that resulted in cross-correlation matrices in which the position of the deposit is indicated by a CCMV. Panel c depicts the cross-correlation between the phase and the template of a 1.0 mm deposit with a CCMV of 0.78. The size of the deposit was determined by comparing the CCMVs obtained by cross-correlation between the image and the templates in the library (panel d); the maximum CCMV indicates the method's estimate of the size of the deposit. Since deposits between 0.9 and 1.1 mm will also be detected with the same maximum CCMV, the estimated size of the deposit is 1.0 ±0.1 mm. The error in the estimated size could be reduced by adding more finely spaced templates to the library.

In the cross-correlation example shown in Figure III-4 panel c, the CCMV of 0.8 indicates that the signature in the image does not exactly match the signature in the template even though both contain the same phase signature of a 1 mm deposit. The decrease in CCMV from 1 (perfect match) to 0.8 is due to the presence of noise in the image. By studying changes in CCMV similar to this one, we determined the influences of various MR parameters and the deposit itself on the method in simulation experiments.
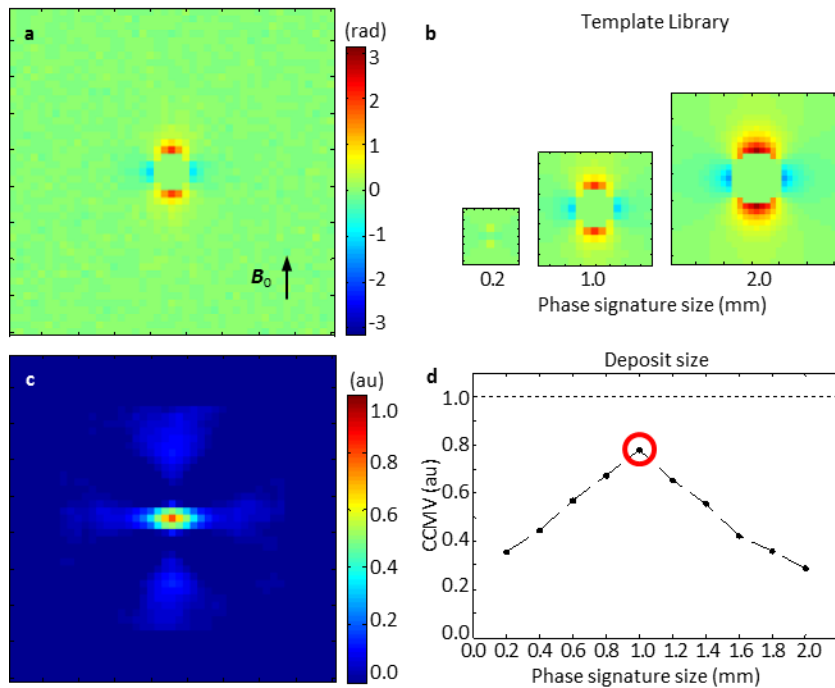
Figure III-4. Detection of calcium deposits *via* cross-correlation method. Cross-correlation between the simulated phase of a deposit (panel a) and a library of templates containing the phase signatures of deposits with various sizes (three shown in panel b) results in cross-correlation matrices (1.0 mm template shown in panel c), where the position of the deposit is indicated by a CCMV, the size of the deposit (1 mm) by a maximum CCMV across cross-correlation matrices (panel d), and the measurement error (±0.1 mm) by step size between deposits used to generate the templates.

Simulating the influences of spatial resolution, deposit size and shape,

and location on cross-correlation

The influence of deposit shape on the method was assessed by comparing the phase signatures of two deposits with different shapes and their corresponding CCMVs. Figure III-5 depicts a high resolution simulation of the phase image of a spherical object (panel a), and a non-spherical deposit (panel b). The shape was obtained from an actual calcium fragment from the CT experiments described in Chapter 4 (section *Computed Tomography*). Both objects are 0.3 mm in the longest dimension. To show the phase

28

signatures in detail, the simulations used voxel sizes of $(0.03 \text{ mm})^3$. There are some differences between both signatures at the boundaries of the deposits; however, the simulated phase signatures of the deposits with a voxel size of $(1 \text{ mm})^3$ (panels c and d), a size more common in clinical MRI, are very similar. Panel c shows the signature generated by the spherical deposit, and panel d depicts the signature of a non-spherical deposit. Even though both signatures can be differentiated at $(0.03 \text{ mm})^3$ spatial resolution, they appear very similar at $(1 \text{ mm})^3$ spatial resolution. In fact, when the cross-correlation method is applied to the lower resolution images, the CCMVs obtained are almost identical, 1.0 for the spherical deposit and 0.9996 for the non-spherical deposit. This result suggests that the method can detect deposits with different shapes in images with lower spatial resolution.

The influence of image SNR on the method's response was determined by comparing the CCMVs obtained when applying cross-correlation to simulated MR phase images of a 1 mm calcium deposit with different levels of noise. Figure III-6 panel a displays the CCMVs obtained when cross-correlation was applied to images generated using $B_0 = 7T$ and a voxel size of $(0.4 \text{ mm})^3$ for SNR values between 5 and 95. The CCMV curve shows an asymptotic recovery starting at 0.5 when the SNR is 5, reaching 90% of its terminal value of 1.0 at an SNR of approximately 20. The 95% confidence interval (CI) of each CCMV (indicated by the error bars) decreased gradually for increasing SNR values; the initial CI range of 0.23 for an SNR of 5 reduced to 0.10 at an SNR of 20. In simulations with voxel sizes of $(0.2 \text{ mm})^3$, a similar CCMV response was obtained. In this case, the recovery started at 0.6 at an SNR of 5 and reached 90% of its terminal mean

value of 1.0 at an SNR of 20. The initial CI of 0.06 for an SNR of 5 reduced to 0.03 at an SNR of 15. The method is influenced by noise in an asymptotic manner with smaller CCMVs and larger CIs for lower SNR values and larger CCMVs and smaller CIs for higher SNRs.
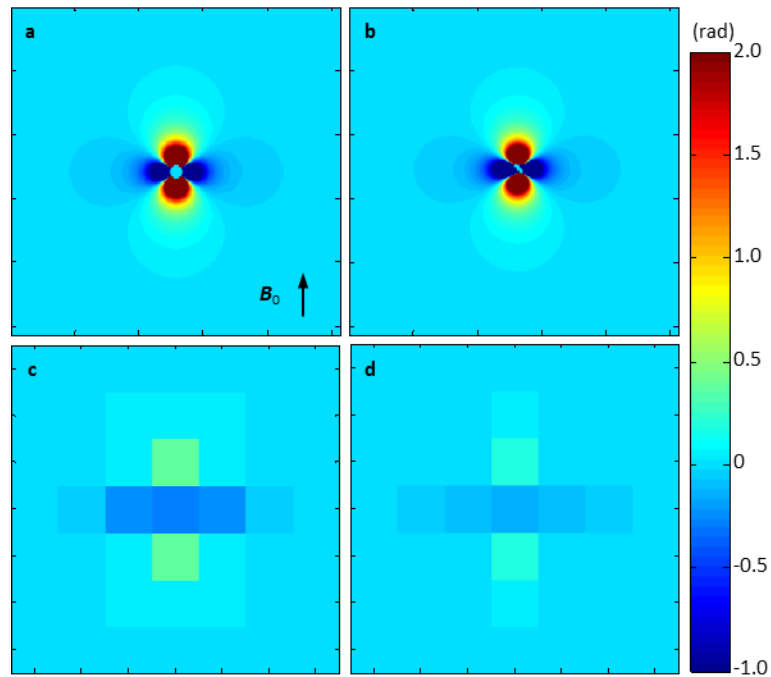
Figure III-5. Phase signatures of spherical and non-spherical deposits. High spatial resolution phase signatures of a spherical (panel a) and non-spherical (panel b) deposit show differences at the boundaries; however, their lower resolution signatures (panel c) and (panel d), respectively, are very similar and cross-correlation detects them with CMMVs of 1.0 and 0.9996, respectively.

The influence of deposit position on cross-correlation was determined by studying changes in CCMV obtained when detecting the deposit at different locations. Figure III-6 panel b shows the CCMVs measured in simulated MR phase images of a 1 mm calcium deposit systematically positioned from the center of a voxel to 1.0 mm, or two and a half times the size of the voxel, in the direction parallel to B_0 in steps of 0.04 mm. The

images were generated using B_0 = 7T and a voxel size of $(0.4 \text{ mm})^3$. The CCMV was the highest (0.98) when the deposit is centered in a voxel (locations 0, 0.4, and 0.8 mm) and the lowest (0.69) when it is between two voxels (locations 0.2, 0.6, and 1.0 mm). The CI was the same (0.018) for the different positions. Similar results were found when the position of the object was changed to the other orthogonal directions. Similar CCMV curves were also obtained in simulations with a voxel size of $(0.2 \text{ mm})^3$. In this case, the minimum CCMV was 0.81 and the CI range was 0.003. Since the template was made with the object centered in a voxel, the largest CCMVs are expected when the deposit is located in the center of the voxel and the results confirm this. In addition, the results indicate that the CCMV range and CI are different for the voxel size and deposit size combination, and that the template and the phase signature are less alike when the deposit is centered right between voxels, indicated by the lowest CCMVs at these locations.

The combined effects of noise and deposit position in the voxel on the method were determined by comparing the CCMVs obtained with images containing deposits at different locations with different SNRs. The CCMVs measured on simulated MR phase images of a 1 mm calcium deposit for different SNR and positions of the deposit are displayed in Figure III-6 panel c. The images were generated using B_0 = 7T and a voxel size of $(0.4 \text{ mm})^3$ with SNR values between 5 and 95. For each SNR value the object was moved in ten equally spaced locations in each dimension, totaling 1000 different locations, within the voxel. The CCMV curve shows an asymptotic recovery starting at

0.43 when the SNR is 5, reaching 90% of its terminal mean value of 0.8 at an SNR of 15.

The CI range remained at 0.2 for all SNR values.
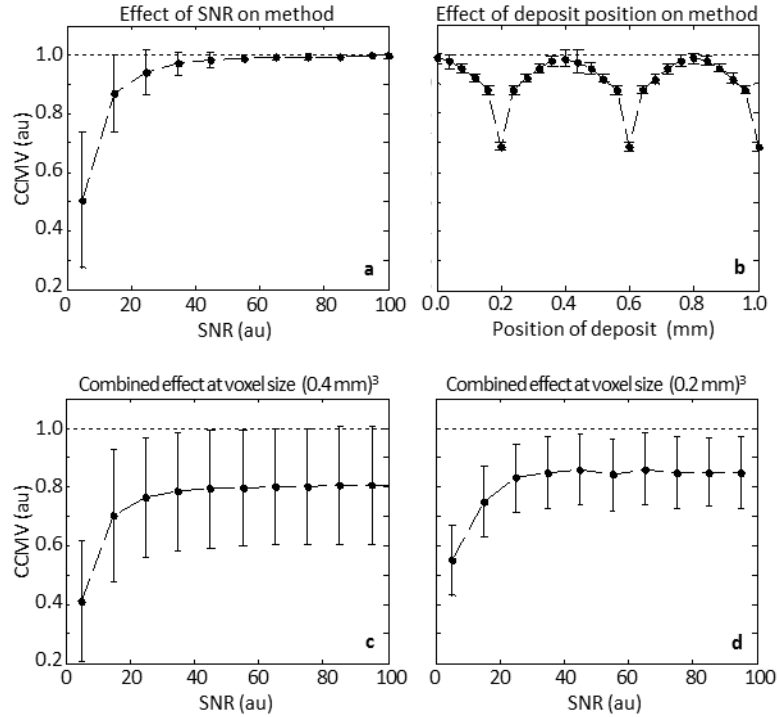
Figure III-6. SNR and partial volume effects on cross-correlation method measured in simulations of a 1mm deposit. CCMV curves obtained for different conditions of (panel a) noise indicates the method's asymptotic response to SNR; (panel b) different positions show fluctuations of CCMV between 0.65 and 1.0; (panel c) varying SNR and position of the deposit yield a terminal CCMV with constant CI when SNR is above 35; (panel d) spatial resolution shows less partial volume effects (increased terminal CCMV and decreased CI) when the resolution increases from $(0.4 \text{ mm})^3$ (c) to $(0.2 \text{ mm})^3$ (panel d).

Similar effects were observed at higher resolution. The CCMVs obtained with images with a voxel size of $(0.2 \text{ mm})^3$ containing deposits with different positions and SNRs are shown in Figure III-6 panel d. The terminal mean CCMV value was 0.85 and the range of the CI was 0.12 across all SNR realizations. There was an increase in terminal CCMV and a decrease in CI when spatial resolution increased from $(0.4 \text{ mm})^3$ to $(0.2 \text{ mm})^3$. These

changes suggest that the terminal CCMV and CI depend on the combination of deposit size and voxel size: larger deposit sizes in images with smaller voxels result in larger terminal CCMVs with smaller CIs.

Discussion

A similar method to the one implemented here has been used for detection of iron-oxide-labeled cells (11). Superparamagnetic iron oxide (SPIO) nanoparticles have a large magnetic susceptibility difference with tissue water, thereby perturbing the local magnetic field over length scales approximately 50 times the particles' dimensions. The distortion has a dipole shape and is recorded in high resolution gradient echo phase images; cross-correlation between the dipole pattern and the phase images indicated the occurrences of the nanoparticles. In the method implemented here, we also used cross-correlation to detect a dipole shape, in this case one generated by a more subtle magnetic susceptibility difference between calcium and tissue water, in MR phase images. In addition, we studied how the method is affected by various MR parameters; understanding these effects will help determine the optimum gradient echo parameters for detecting calcium deposits in practice. In simulation experiments, we quantified the partial volume effects and determined the *TE* needed to obtain detectable phase signatures of deposits of different sizes for typical spatial resolutions. (i.e. Table III-1). These results indicate that we can only detect deposits of certain sizes when using a fixed *TE* and that the size depends on the spatial resolution. For instance, when using a *TE* = 12.5 ms we should be able to detect calcium deposits with the same size as the

voxel size. Therefore, if we wish to detect deposits of different sizes, we need to acquire images using multiple *TE*s.

Another practical result obtained by simulation is the method's response to varying SNR. We learned that after a SNR of 30, the SNR effects on cross-correlation are minimal (see Figure III-6); thus, if our current acquisition parameters produce images with SNR of 100, we can use a new set of parameters to trade SNR for higher spatial resolution, which increases the terminal CCMV and reduces the CI thereby increasing our ability to detect the dipole. However, this new set of parameters needs to produce images with a SNR above 30.

Our simulation experiments also led to another practical result on the method's ability to characterize spherical deposits in images of different spatial resolutions (see Figure III-6). These values can be used as a reference to determine if a spherical calcium deposit is present in an image or not. For example, if we obtain a CCMV of 0.8 with a template generated with a 1.0 mm deposit when performing cross-correlation between a template library and a phase image with voxel size of $(0.4 \text{ mm})^3$ and SNR of 50, we can determine with confidence that there is a 1.0 mm deposit in the image.

Before estimating the range of CCMVs needed to detect microcalcifications in breast MR phase images, the technique needs to be verified in phantoms and refined to detect typical microcalcifications found in human breast tissue. The shapes and configurations of actual microcalcifications and the presence of other anatomical structures in close proximity will alter the phase signatures of the microcalcifications and reduce the CCMVs. While we quantified the effect of noise, location of the object, and resolution,

we still need to address the effects of the shapes of microcalcifications and presence of other nearby anatomical structures nearby on cross-correlation.

The simulations also provided insight on the method's specificity. We found that deposits with different shapes are detected with very similar cross-correlation indices; in images with voxel sizes larger than the deposit size (see Figure III-5). This suggests that the method has intrinsic low specificity. Since distinguishing the different shapes of microcalcifications associated with benign and malignant tumors is of central importance in diagnosing breast cancer, the clinical value of the method will be reduced.

CHAPTER IV

VALIDATION OF CALCIUM DEPOSIT DETECTION WITH CROSS-CORRELATION IN

PHANTOMS

<u>Introduction</u>

In Chapter III we described the implementation and testing of cross-correlation using

simulated MR data of calcium deposits; we evaluated the method's response to

different conditions of noise, spatial resolution, and position of the deposit within the

voxel and we determined the MR parameters, SNR, and CCMV needed to detect

spherical calcium deposits. In this chapter we aim to validate the findings in Chapter III

using experimental MRI of phantoms. In particular, we validated the cross-correlation

responses under different conditions of noise, resolution, and position using a spherical

calcium-like deposit immersed in gel.

Using the MR parameters and the appropriate SNR determined by simulation, we

acquired images of actual calcium fragments of different sizes and shapes immersed in

gel, applied cross-correlation to detect the deposits, and employed receiver operator

characteristic (ROC) analysis to determine the cross-correlation cut-off values needed to

optimize the sensitivity and specificity of the method. Additionally, we tested the

method in a more realistic phantom; we applied cross-correlation to MRI images of

chicken breast phantoms containing calcium-like deposits. We used computed

tomography (CT) In order to measure and verify the location of the deposits.

Measurements of SNR, deposit position, and spatial resolution effects on cross-

correlation in phantom experiments

The influences of spatial resolution, SNR, and deposit location on the method determined through simulations were measured and validated in MR images of a phantom mimicking a calcium deposit within tissue. The phantom consisted of a 1 mm borosilicate glass bead (Aldrich, St. Louis, Missouri) immersed in agar gel. The bead was chosen because it has a spherical shape and, like calcium, has very low water content and a magnetic susceptibility of $\chi = -11 \times 10^{-6}$ (27). Similarly, agar gel was used because it has the same magnetic susceptibility ($\chi = -9 \times 10^{-6}$) as tissue. MR images were acquired using a Varian scanner (Palo Alto, CA) at a magnetic field strength 7T using a 3D gradient recalled echo pulse sequence with $TR/\alpha = 10$ ms/7° at two spatial resolutions. Images with voxel sizes of $(0.2 \text{ mm})^3$ were acquired with a $TE = 1.35$ ms and a bandwidth of 1330 Hz/pixel while images with voxel sizes of $(0.4 \text{ mm})^3$ were acquired with $TE = 1.31$ ms and a bandwidth of 2666 Hz/pixel. The FOV and acquisition matrix were varied to obtain these spatial resolutions and the number of acquisitions was systematically increased to achieve different SNR values.

The influence of deposit location on the method was determined experimentally by comparing the CCMVs obtained from images with different positions of the object relative to the center of the FOV. The deposit location was not changed; rather, the offset in the readout direction was modified to obtain images with different positions

relative to the deposit, this is equivalent to moving the deposit within the FOV. In MR images of the phantom acquired at 7T with isotropic voxel sizes of 0.2 mm, different positions of the deposit within the FOV were obtained by systematically increasing the offset of the center of the FOV. The offset was increased from 0 to 0.8 mm in steps of 0.02 mm. For each position, six images were acquired. Cross-correlation was applied to the images to locate the deposit and the mean CCMV and standard error were measured.

The effects of spatial resolution, SNR, and deposit location on the method were measured by studying the changes in CCMV obtained when detecting the calcium-like deposit in MR phase images of the phantom acquired with isotropic voxel sizes of $(0.2 \text{ mm})^3$ and $(0.4 \text{ mm})^3$, different SNR, and different positions of the deposit. For each combination of voxel size, the influences of both SNR and the location of the deposit were determined. MR images of the phantom were obtained in three different scan sessions. On each occasion, the phantom was adjusted to assure that the deposit was in a different location, and images with different SNR values were obtained by adjusting the number of repetitions to 1, 2, 4, 8, 16, and 32. Cross-correlation was applied to the images to locate the deposit and the mean CCMV and standard error were measured.

High-pass filtering experiments

Before computing the cross-correlation between the experimental data and the template, a high-pass spatial frequency filter was applied to the phase images to remove the slowly varying phase artifacts (28). Briefly, this filter attenuates low-

38

frequency variations by applying a $N \times N \times 1$ low pass Hanning filter to the original k-space data followed by complex division of the original k-space data by the low-pass filtered k-space. The size N of the filter was determined empirically by testing filters with sizes between 3 and 71, in steps of 2, and qualitatively comparing which filter removed the most of artifacts while also keeping the phase signature of calcium deposits.

The influence of filter size on the method's response was determined by comparing the CCMVs obtained with experimental and simulated MR images of a 1 mm calcium deposit filtered with different filter sizes. The simulated images of 1 mm calcium deposit were generated at 7T with voxel sizes of $(0.2 \text{ mm})^3$ and SNR of 50. The experimental images of a 1 mm glass bead immersed in gel were acquired with a Varian 7T scanner using 3D gradient recalled echo pulse sequences with TR/α= 10 ms/7$^\text{o}$, TE=1.35 ms, bandwidth of 1330 Hz/pixel, and voxel size of $(0.2 \text{ mm})^3$. The number of acquisitions was empirically adjusted to achieve a SNR of 50. Simulated and experimental images were filtered with $N \times N \times 1$ low pass Hanning filters with N sizes between 3 and 71, in steps of 2. Cross-correlation was applied to the images to locate the deposit and the CCMVs were measured and tabulated.

Sensitivity and specificity of the method for detecting calcium fragments

The sensitivity and specificity of the method for detecting calcium deposits were measured using MR images of phantoms containing calcium fragments. Four phantoms (C1, C2, C3, C4) were constructed, each containing 6-11 fragments (each < 1 mm in the longest dimension) of calcium hydroxyphosphate (Aldrich, St. Louis, Missouri) immersed

in agar gel. The exact dimensions of each fragment were measured with high resolution CT after the phantoms were built. MR images of the phantoms were acquired using a 7T Varian spectrometer using 3D gradient recalled echo pulse sequences with voxel sizes between $(0.2 \text{ mm})^3$ and $(1.0 \text{ mm})^3$, in steps of $(0.2 \text{ mm})^3$. In order to detect the phase signatures of deposits of different sizes on images acquired with the same spatial resolution, various TEs were used according to Table III-1. After setting TE, TR was set to the minimum allowed by the scanner, bandwidths were set to the maximum allowed by the scanner, and the flip angle (α) was determined using the Ernst equation. The number of acquisitions was set to 1, except for images with voxel sizes of $(0.2 \text{ mm})^3$, where the number of acquisitions was set to 8 in order to obtain SNR above 30 (SNR effects on cross-correlation are minimal when SNR>30; see chapter III). Cross-correlation was applied to the images to locate fragments in phantoms C1-C4 and ROC analysis was applied to the CCMVs obtained for each fragment to determine the cross-correlation index cut-off needed to determine the sensitivity and specificity of the method.

When detecting calcium fragments *via* cross-correlation, the presence of a deposit is indicated by a CCMV in the similarity matrices. However, the exact threshold for deciding whether there is a deposit or not is not immediately obvious. To address this issue, we performed ROC curve analysis to determine an optimum cross-correlation cut-off that maximizes sensitivity and specificity. In addition, the area under the curve (AUC) of the ROC curve provided a measure of the performance of the method. Cross-correlation index cut-off values between $0 - 1.0$ in steps of 0.1 were used to determine

ROC values. For each cut-off, the CCMVs obtained from the similarity matrices were diagnosed as positive if the CCMV was equal or above the cut-off, or negative if the CCMV was below the cut-off. A positive diagnosis means that in a specific location there is a calcium deposit present while a negative diagnosis indicates that there is no deposit present. The diagnoses were then compared to the actual size and position of the deposit measured with CT, and each diagnosis was assigned to one of four categories: true positive (TP), which represents a positive diagnosis that was correct; true negative (TN), which represents a negative diagnosis that was correct; false positive (FP), which represents a positive diagnosis that was incorrect; and false negative (FN), which represents a negative diagnosis that was incorrect. Sensitivity and specificity were computed as TP/(TP + FN) and TN/(TN + FP), respectively. The cut-off value that maximized the sum of sensitivity and specificity was chosen. The ROC curve was generated by plotting the true positive rate (TPR) vs the false positive rate (FPR); TPR is equal to the sensitivity and FPR is equal to 1- specificity.

Identifying calcium-like deposits within a tissue like phantom

MR images of a chicken breast phantom containing calcium-like glass beads were acquired to test the cross-correlation method. The beads were inserted approximately 1 cm into the chicken breast through a channel made with the tip of a #80 industrial sewing needle. The sample was then inserted into a glass bottle and the remaining space was filled with saline. MR images of the chicken breast phantom were acquired using a Varian scanner at a magnetic field strength of 7T using a 3D gradient echo pulse

sequence with TR/α= 10 ms/7° at two spatial resolutions. Images with voxel sizes of (0.2 mm)^3 were acquired with TE = 1.35 ms and a bandwidth of 1330 Hz/pixel while images with voxel sizes of (0.4 mm)^3 were acquired with TE = 1.31 ms and a bandwidth of 2666 Hz/pixel. For each spatial resolution, the number of acquisitions was empirically adjusted to achieve a SNR of 50. Cross-correlation was applied to the images to locate the calcium-like deposits. CT was also performed on the phantom to validate the findings obtained by the cross-correlation method.

Computed Tomography

CT images of phantoms C1-C4 were acquired using a Scanco Medical microCT50 (Brüttisellen, Switzerland). CT data were acquired with a tube voltage of 55 kVp, exposure time of 300 ms, an anode current of 0.2 mA, one thousand projections acquired over 180 degrees, and a longitudinal resolution of 10 μm. 2D images were reconstructed from the projections. Then multiple images from adjacent slices were used to reconstruct a three-dimensional volume with isotropic voxel size of (10 μm)^3. Calcium and background gel appeared with different signal intensities, so threshold based segmentation was applied to mask calcium from gel. The Matlab function 'BWCONNCOMP' was applied to the binary image to identify all the connected components, their locations, dimensions (length, width, and height), and shapes.

CT images of the chicken breast phantom were acquired using a Scanco Medical (Brüttisellen, Switzerland) microCT40. CT data were acquired with a tube voltage of 45 kVp, exposure time of 300 ms, an anode current of 177 μA, five hundred projections

42

acquired over 180 degrees, and a z-axis resolution of 30 μm. 2D images were reconstructed from the projections. Then multiple images from adjacent slices were used to reconstruct a three-dimensional volume with isotropic voxel size of $(30 \ \mu m)^3$. CT images were co-registered to MR images using previously established software (29).

<div align="center">Results</div>

<div align="center">*Measuring the effects of deposit position, SNR, and spatial resolution*</div>

<div align="center">*on cross-correlation in phantom experiments*</div>

The influences of deposit position, SNR, and spatial resolution on cross-correlation were measured experimentally using MR images of a 1 mm calcium-like deposit in gel.

Figure IV-1 depicts a picture of the phantom (panel a) and its corresponding MR images (panels b-f). In the magnitude image (panel b) there is a circular signal void generated by the deposit and in the phase image (panel d) the deposit's characteristic dipole shape is present within the slowly varying phase artifacts (due to gel/air interfaces and subtle shimming errors). The artifacts were removed with a high-pass frequency Hanning filter with size 21×21×1 (described in the *High-pass filtering experiments* section); the phase image after filtering shows a clean phase signature of the deposit (panel e), magnified views of the inset show in more detail the signal void (panel c) and the phase signature (panel f).

The influence of deposit location on the method's response was determined experimentally by comparing the CCMVs obtained from images of a 1 mm calcium

<div align="center">43</div>

deposit with different positions relative to the center of the FOV. Figure IV-2 panel a

shows the CCMVs measured on MR images of a 1 mm calcium-like deposit in gel with

readout offsets from 0 to 0.5 mm in steps of 0.02 mm. MRI was performed at 7T and the

images had a voxel size of $(0.2 \text{ mm})^3$. The CCMV plot shows a cyclical shape with a

period equal to 0.2 mm, the size of the voxel. The same maximum of 0.92 was reached

when the offset had values of 0.12 mm and 0.32. Similarly, the minimum (0.78) was

found when the offset had values of 0.02 mm, 0.22 mm, and 0.42 mm. The cyclical
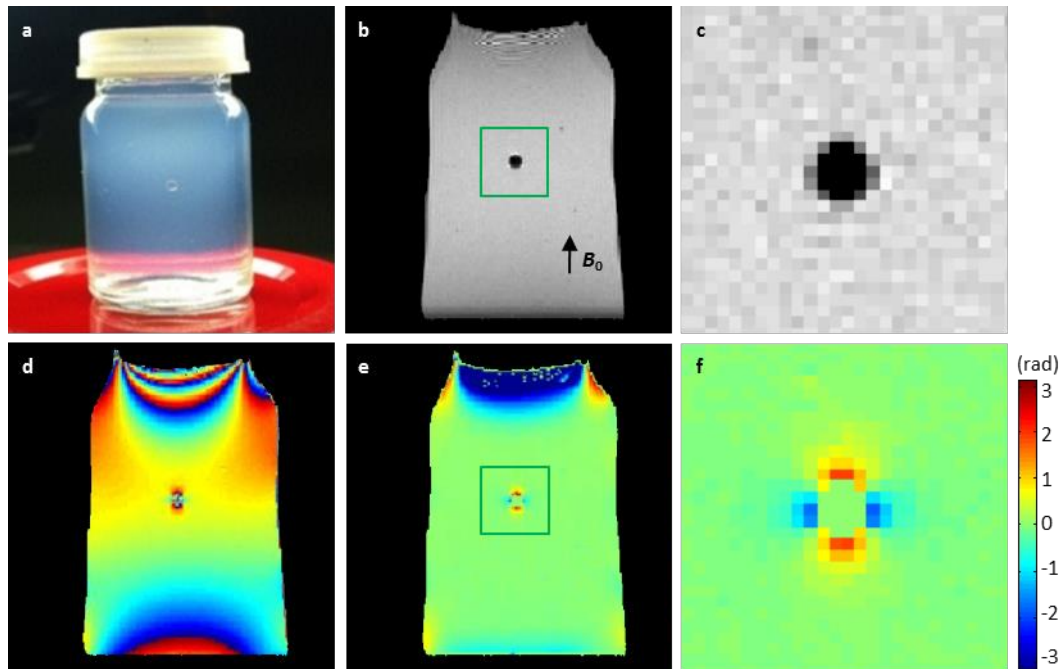
Figure IV-1. MRI of a 1 mm calcium-like object immersed in agar gel. Photograph of the phantom containing a 1 mm glass bead within gel (panel a), the corresponding gradient echo magnitude image shows a signal void created by the deposit (panel b) while the corresponding phase image shows the phase signature of the deposit altered by air/gel interface phase artifacts (panel d). The phase image after high-pass Hanning filtering shows a clean phase signature of the deposit (panel e), magnified views of the inset show in more detail the signal void (panel c) and the dipole shaped phase signature of the deposit (panel f).

shape found experimentally matches that previously observed with simulations (see Figure III-4 panel b). This result validates the findings in simulations: the CCMV depends on the location of the deposit within the voxel; the largest CCMVs are expected when the deposit is located in the center of the voxel while the smallest CCMVs are expected when the deposit is located off center.
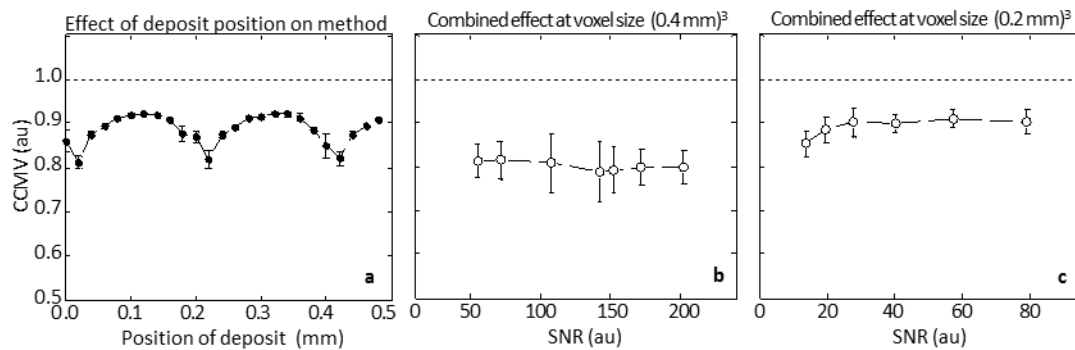
Figure IV-2. SNR and partial volume effects on cross-correlation method measured in gel phantom containing a 1mm calcium-like deposit. Panel a shows the CCMV curve obtained for different positions of the deposit indicates fluctuations of the CCMV between 0.81 and 0.93; Panels b and c indicate increased terminal CCMV and decreased CI when spatial resolution changes from $(0.4 \text{ mm})^3$ (panel b) to $(0.2 \text{ mm})^3$ (panel c). Panel c illustrates the method's asymptotic response with a terminal CCMV of 0.91 when SNR is above 25;

Figure IV-2 depicts the influences of deposit location and image SNR on the method's response, determined experimentally by comparing the CCMVs obtained from images of a 1 mm calcium-like deposit with different positions and SNRs. Panel b displays the CCMVs obtained when cross-correlation was applied to images with voxel size of $(0.4 \text{ mm})^3$ for SNR values between 50 and 200. Panel b shows CCMVs obtained when cross-correlation was applied to images with a voxel size of $(0.4 \text{ mm})^3$ for SNR values between 50 and 200. The CCMV shows a relative constant value of 0.81 with a CI

45

of 0.05 (indicated by the error bars). The asymptotic CCMV recovery, found in simulations, is not evident in this plot because lower SNR measurements are missing; images with spatial resolution of $(0.4 \text{ mm})^3$ did not have a SNR below 50. Panel c displays the CCMVs obtained with spatial resolution of $(0.2 \text{ mm})^3$; the CCMVs obtained with these images showed the asymptotic shape starting at 0.85 when the SNR was 12, reaching 90% of its terminal value of 0.91 at an SNR of 25 and a CI of 0.023. The effect of spatial resolution on the method was measured by comparing the CCMVs obtained at different spatial resolutions. The CCMVs obtained with images with a voxel size of $(0.4 \text{ mm})^3$ (panel b) have lower terminal mean CCMVs and larger CIs than those obtained with images with voxel size of $(0.2 \text{ mm})^3$ (panel c). These results support the findings of the simulations: terminal CCMVs and CIs depend on the combination of deposit size and voxel size; and larger deposit sizes in images with smaller voxel sizes result in larger terminal CCMVs with smaller CIs.

Measurement of high-pass filtering effects on cross-correlation

The influence of filter size applied to the MR phase images was determined by comparing the CCMVs obtained when applying cross-correlation analysis to detect a 1 mm spherical deposit in MR images processed with $N \times N \times 1$ low pass Hanning filters with different N sizes. Figure IV-3 shows the CCMVs obtained with simulated images of a 1 mm calcium deposit surrounded by tissue and two experimental images of a 1 mm calcium like deposit surrounded by gel filtered with low pass Hanning filters with sizes N between 3 and 71. In experimental and simulated images, filters with sizes $N < 11$

reduced CCMVs. In experimental images, filters with N>51 also reduced CCMVs. Filters

that did not affect cross-correlation had sizes between 11 and 51.
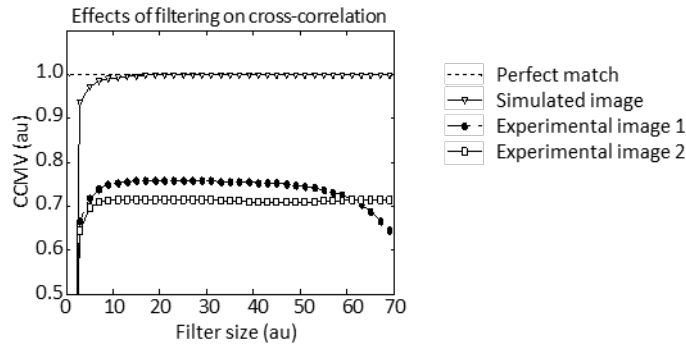
Figure IV-3. Effects of high-pass filtering on cross-correlation. Changes on CCMVs between a template (not filtered) and images of a deposit after applying a [N×N×1] high-pass spatial frequency filter indicate that filters with N values between 11-51 did not affect cross-correlation.

Detection of calcium fragments with cross-correlation

Cross-correlation analysis was applied to MR phase images of the phantoms (C1, C2,

C3, and C4) to detect calcium fragments in images acquired with different spatial

resolutions. Figure IV-4 shows the detection of a deposit in images of phantom C1 with

voxel size of $(0.4 \text{ mm})^3$. In the magnitude image (panel a) there is a signal void

presumably created by the calcium fragment. In the phase image (panel b) there is a

negative region surrounding the location of the signal void but the dipole shaped phase

signature is not evident and identification of the deposit directly from this view not

possible. Cross-correlation between the phase image and a template generated with a

0.5 mm deposit, however, indicates the presence of a calcium deposit in the same

location of the signal void with a CCMV of 0.68 in the similarity matrix (panel d). The CT

47
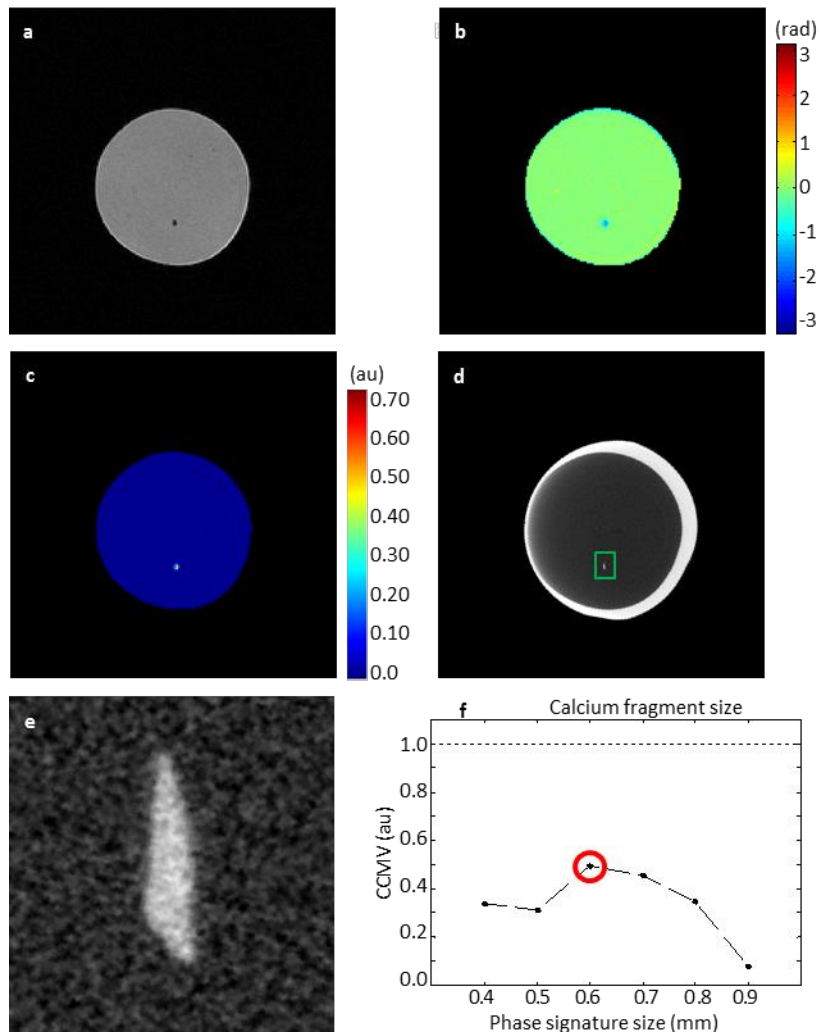
Figure IV-4. Calcium fragment detected *via* cross-correlation. Magnitude (panel a) and phase (panel b) images of phantom C1 suggest the presence of a calcium fragment while cross-correlation indicates the presence of a deposit, indicated by a CCMV of 0.68 in the similarity matrix (panel c). This finding is confirmed by the presence of a calcium fragment in the corresponding CT image (panel d); a magnified view of the inset in the CT image shows the non-spherical shape of the fragment. The size of the fragment is determined in the plot of CCMVs obtained from the phase image and templates generated with deposit sizes between 0.4 -0.9 mm (panel f). The estimated size of 0.6 mm of the detected deposit is indicated by the maximum CCMV across the templates and the uncertainty by the difference between phase signature sizes in the library. In this case, it is ±0.05 mm.

image of phantom C1 (panel c) confirms the presence of a calcium fragment deposit in the same location of the signal void. Since there is a CCMV, the phase signature must be a dipole even though we can only see a negative region. This can be explained by orientation of the dipole, which has positive lobes parallel to B_0; in this case, the dipole is perpendicular to the page. Since the positive lobes are perpendicular to the page, only one lobe, positive or negative, can be seen in the phase image view; in this case we are seeing the negative lobe. The dipole shape should be evident in the plane perpendicular to the page. This example illustrates how cross-correlation is not affected by the orientation of the dipole in the image; as long as the template is generated with the same orientation with respect to B_0, detection of the deposit is feasible.

From the simulations in Chapter III (*Simulating the influences of spatial resolution, deposit size and shape, and location on cross-correlation*), we learned that different deposit shapes can create a dipole shaped phase signature; this finding is validated in the experiment described in Figure IV-4. The magnified view of the inset in the CT image (panel c) shows the non-spherical shape of the deposit and the CCMV of 0.68 indicates a dipole shaped phase signature.

The size of the calcium fragment measured *via* cross-correlation is similar to that obtained with CT. In CT data the length, width, and height of the fragment were measured as 0.52×0.37×0.75 (mm) and the mean dimension as 0.55 mm. The measurement of the fragment size with cross-correlation is illustrated in Figure IV. Panel f shows the plot of the CCMVs obtained with cross-correlation between the image and a library of templates generated with deposit sizes between 0.4 and 0.9 mm. The size of

the detected deposit is 0.6 mm, indicated by the maximum CCMV across phase

signature sizes. Since deposits with sizes between 0.55 and 0.65 mm will also be

detected with the same maximum CCMV, the uncertainty of the deposit size

measurement is ±0.05 mm. The size of the deposit measured with cross-correlation

analysis is 0.6 ±0.05 mm, which is very close to that measured with CT (0.55 mm).

a	ROC analysis	
CCMV CUTOFF	Sensitivity (TPR)	Specificity (1-FPR)
0.00	1.00	0.00
0.10	1.00	0.12
0.20	0.94	0.40
0.30	0.94	0.58
0.40	0.76	0.69
0.50	0.59	0.77
0.60	0.53	0.88
0.70	0.29	0.97
0.80	0.12	1.00
0.90	0.00	1.00
1.00	0.00	1.00
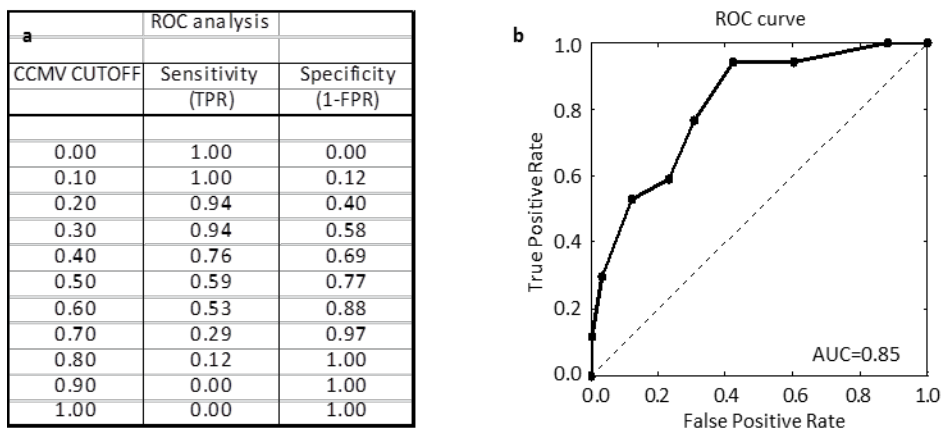
Figure IV-5. ROC curve analysis applied to detection of calcium fragments *via* the cross-correlation method. In the ROC analysis, CCMV was used as the discrimination threshold to determine if a fragment was present or not; different CCMV cut-off values were used to compute sensitivity, specificity, TPR, and FPR (panel a), and the ROC curve was generated using FPR and TPR (panel b). The AUC (0.85) indicates moderate discriminatory power, better than chance (AUC = 0.5).

ROC analysis was applied to the CCMVs obtained from cross-correlation analysis on

phantoms C1-C4 in order to determine the optimum cross-correlation cut-off (for

determining whether there is a deposit or not) and the corresponding sensitivity and

specificity for detecting all of the calcium fragments. Figure IV-5 illustrates the ROC

curve analysis applied to the method for detecting calcium fragments with a size range

between 0.14 mm and 0.79 mm on images acquired with voxel size of $(0.4 \text{ mm})^3$. Panel

a shows a table with the cut-off values and their corresponding sensitivity and specificity. Low cut-off values have high sensitivity and poor specificity, while high cut-off values have low sensitivity but high specificity. The cut-off chosen was 0.4 because it provides high and similar sensitivity (76%) and specificity (69%). Panel b depicts the ROC curve with an AUC of 0.8 indicating moderate discriminatory power. (Recall that chance results in an AUC = 0.5).

	Table IV-1 ROC analysis of detection of calcium fragments in gel *via* cross-correlation		
	Sensitivity (%), specificity (%), AUC		
Deposit size (mm)	Image voxel size (mm)^3		
	0.2	0.4	0.6
0.2	71, 50, 0.60	X	X
0.3	90, 52, 0.77	X	X
0.4	89, 51, 0.85	78, 68, 0.88	X
0.5	X	75, 67, 0.84	50, 68, 0.74
0.6	X	67, 67, 0.70	67, 80, 0.86
"X" indicates combinations with unavailable TE (too short) or combinations producing very low SNR images (TE too long).			

In order to determine the sensitivity and specificity of the method for detecting calcium fragments of specific size in images with different spatial resolutions, ROC analysis was applied to the method for detecting calcium fragments with sizes between 0.2 and 0.6 mm, with a step size of 0.1 mm, in images with voxel sizes of (0.2 mm)^3, (0.4 mm)^3, and (0.6 mm)^3. Table IV-1 shows the sensitivity and specificity for the detection

of calcium fragments for different combinations of deposit size and image spatial resolution.

Identifying calcium-like deposits within a tissue like phantom

Figure IV-6 illustrates the detection of calcium like deposits (GB1 and GB2) within chicken breast tissue *via* the cross-correlation method. While both were detected, for simplicity only GB1 is shown. Panels a and b display MR magnitude and phase images, respectively; panel c is the cross-correlation matrix and panel d shows the CT image. Panels e-h depict the enlarged views in the green inset for panels a-d, respectively. In the gradient echo magnitude image, the location of GB1 can be any region with a circular signal void; however, a signal void can also indicate the location of an air bubble. The possible locations of the deposit are indicated by the arrows in panel e. Similarly, in the phase image, the location of GB1 can be indicated by its dipole shape signature, but there are also other dipole shapes generated by air bubbles and 2D dipole shapes generated by blood vessels orthogonal to the slice. The signature of the deposit, however, can be identified by the polarity of the dipole (positive lobe parallel to the main magnetic field and negative shifts perpendicular to the main magnetic field); the phase signature of GB1 is indicated by the white arrow while the phase signatures of air bubbles are indicated by black arrows in panel f. In the similarity matrix, the location of GB1 is clearly indicated by a cluster of cross-correlation values above 0.5, and the exact location indicated by the CCMV (0.73). In the CT image, the location of GB1 is evident and corroborates the location found   *via* cross-correlation. GB1 had a CCMV of 0.73,

52

Figure IV-6. **Detection of a calcium-like deposit within tissue *via* cross-correlation.** MR magnitude (panel a) and phase images (panel b) of chicken breast containing a 1 mm glass bead do not indicate the presence of the bead while the cross-correlation matrix (panel c) reveals the deposit's presence and position, which were validated by CT (panel d). Panels e-h depict the enlarged views of panels a-d respectively. In the green inset in panel a, white arrows indicate the location of the bead while black arrows indicate the location of air bubbles. The magnified view of the magnitude image (panel b) also indicates the presence of structures adjacent to the bead that alter the dipole shape of the deposit phase signature (panel d).

which is within the range determined by simulations [0.70, 1.0], but GB2 had a CCMV of

0.40. The smaller CCMV for GB2 can be explained by the presence of other small

structures near the bead that appear as signal voids (panel e). These structures alter the

phase signature of the glass bead (panel f), rendering it less similar to the template and

therefore decreasing the CCMV.

Similar results were obtained in another experiment with a chicken breast phantom

containing three glass beads (GB3, GB4 and GB5). In this experiment, the MR data was

acquired at two different resolutions using voxel sizes of $(0.4 \text{ mm})^3$ and $(0.2 \text{ mm})^3$. In

both cases GB4 and GB5 were located while GB3 was outside the FOV and was not

detected. Figure IV-7 shows the detection of the beads in MR images with $(0.2 \text{ mm})^3$

voxel size. In the magnitude image (panel a), the location of GB4 and GB5 is not evident;

it may be any circular signal void. Similarly, in the phase image (panel b) there are a few

phase signatures, especially in the tissue close to the tissue/air interface, suggesting the

presence of calcium-like deposits. In the similarity matrix (panel c), the location of both

deposits is revealed by CCMVs of 0.74 for GB4 and 0.35 for GB5. GB5 was surrounded by

a partially closed tunnel and, therefore, resulted in a lower CCMV. The location of both

deposits was confirmed by the presence of the glass beads in the corresponding CT

image (panel d). For the images acquired with voxel sizes of $(0.4 \text{ mm})^3$, the beads were

detected with a CCMV of 0.49 for GB4 and 0.19 for GB5. Just as in the simulations of

chapter III, the CCMVs were lower in images with $(0.4 \text{ mm})^3$ voxel size than in images

with $(0.2 \text{ mm})^3$ voxel size. The locations of the beads were also validated by CT. As in the

previous experiment, the smaller value of CCMV for GB5 was due to the presence of a

tunnel similar to the structure affecting GB2.
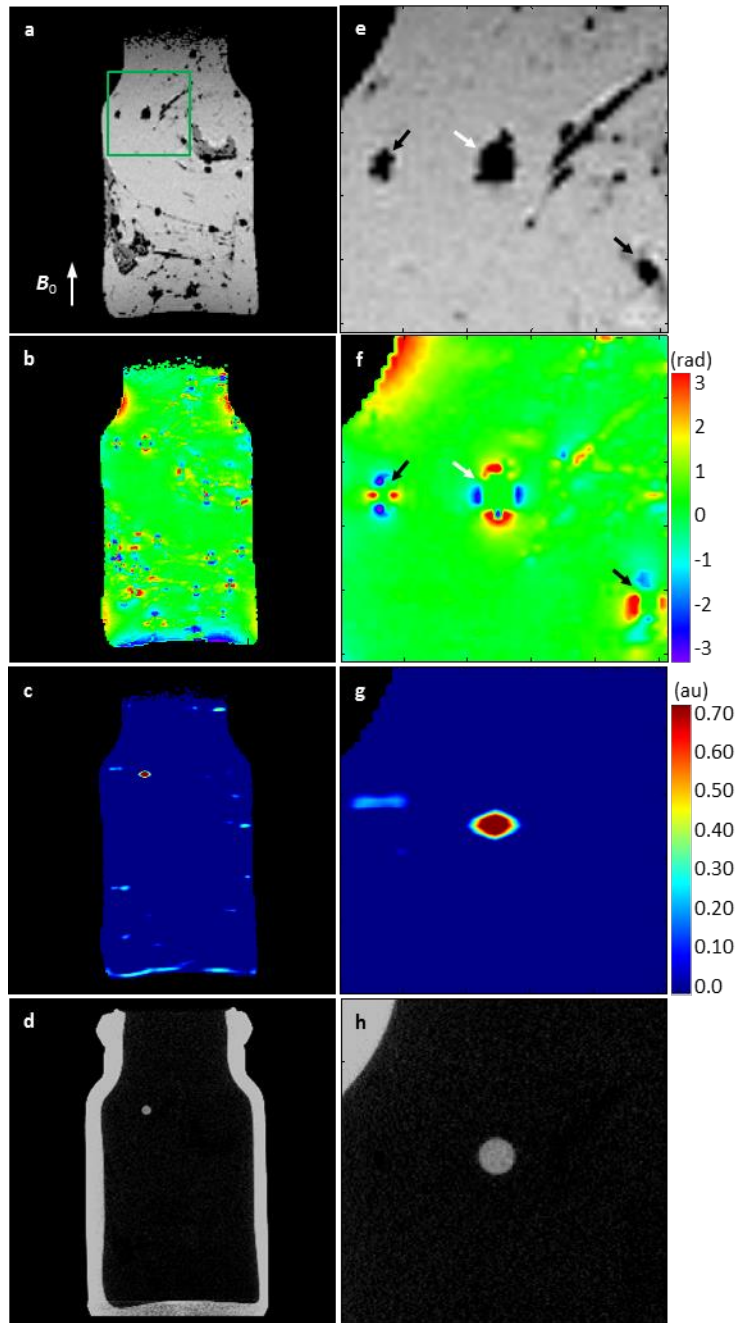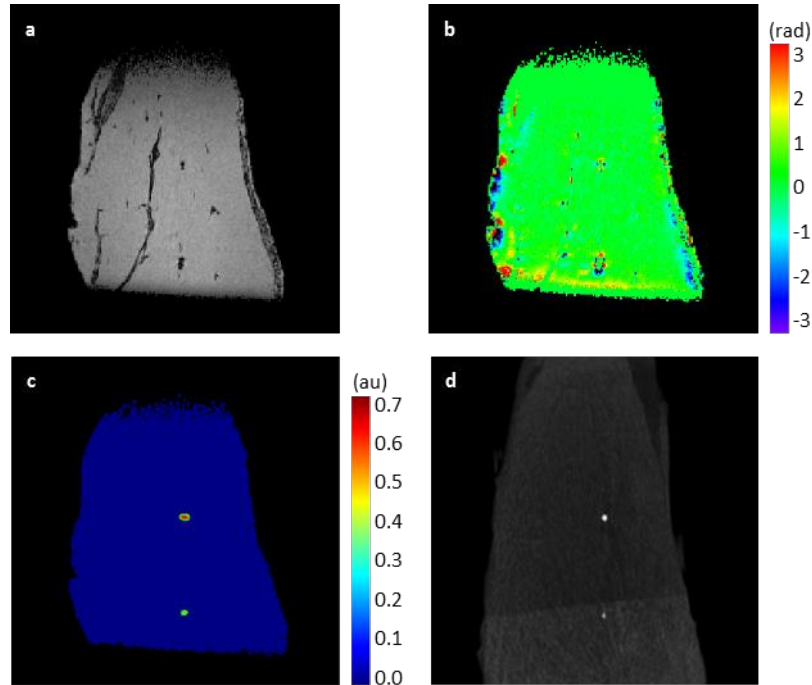

Figure IV-7. Detection of calcium-like deposits within tissue *via* the cross-correlation method. MR magnitude (panel a) and phase images (panel b) of chicken breast containing two 1mm glass beads do not indicate the presence of the bead while the cross-correlation matrix (panel c) reveals the presence and position of the deposits, validated by CT (panel d).

Discussion

The experiments performed in this chapter helped to validate the findings from

simulations. In particular, the method's response to SNR, position of the deposit, and

spatial resolution was validated. Additionally, these experiments also identified some

practical implementation challenges not considered during simulations. During

simulations, the *TE*s needed to detect deposits of different sizes in images with different

spatial resolutions were computed and summarized in Table III-1; however, not all of

these values were practical. Some small *TE* values were not available in gradient echo 3D for certain spatial resolutions (see Table IV-1). Other *TE* values were too large and produced images with very low SNR that are impractical in cross-correlation. Acquisition time was kept as low as possible by using the minimum TR allowed in gradient echo 3D imaging. However, when increasing the *TE*, TR needed to be increased and this increased acquisition time. All of the experimental images needed to be high-pass filtered. We anticipated this need and measured the effect of the filter size on cross-correlation for spherical calcium-like deposits surrounded by gel to determine the range of filter sizes that did not affect detection *via* cross-correlation.

When detecting calcium fragments of different sizes and shapes we found some differences and similarities between the sizes measured by CT and cross-correlation (i.e. Figure IV-4). From the CT images, it was possible to measure the length, width, and height of each fragment; for instance, the deposit shown in Figure IV-4e has dimensions of 0.52×0.37×0.75 (mm^3). With cross-correlation, however, only one dimension can be measured. The dimension measured corresponds to the diameter of the spherical deposit in the template used to detect the calcium fragment; in the case illustrated in Figure IV-4f it was 0.6 mm. We found empirically that this measurement matches the mean of the length, width, and height measured in CT images.

In X-ray mammography, the size of the fragment will depend on its orientation with respect to the detector and the X-ray source, assuming that there is no apparent amplification by X-rays. For instance, if the object's largest dimension is perpendicular to the detector, this dimension will not be recorded and the fragment will look smaller, in

the case of the aforementioned fragment with dimensions 0.52×0.37×0.75 (mm^3), it will appear to be 0.52×0.37 (mm^2); however, if the object's smallest dimension is perpendicular to the detector, this dimension will not be recorded and the fragment will look bigger, in the case of the fragment aforesaid, it will appear to be 0.52×0.75 (mm^2). Unlike X-rays, the sizes of the fragments measured *via* cross-correlation do not depend on their orientation and match the mean average of the deposit.

Detection of calcium-like deposits within tissue was more challenging than detecting deposits within gel. We obtained CCMVs of 0.91 when detecting 1 mm glass beads within gel in images with voxels size of (0.2 mm)^3; however, the CCMV range obtained when the deposit was within tissue was [0.34, 0.70] (see Figures IV-2, IV-6, and IV-7). The decrease in CCMVs was due to presence of structures adjacent to the bead that altered the dipole shape of the deposit phase signature. In addition, chicken breast tissue is not as homogenous as gel and produced more phase variations, which also reduced the cross-correlation indices.

In this chapter, the influences of deposit position, SNR, and spatial resolution on cross-correlation were measured experimentally using a spherical calcium-like deposit immersed in gel; the effects found matched those determined by simulation in Chapter III. Also, because the experimental MR phase images required high-pass filtering, the effects of the filter on cross-correlation were measured and the filter sizes that did not affect the method were determined. In addition, cross-correlation was used to detect calcium fragments with different shapes within gel and calcium-like deposits within chicken tissue. In both experiments, the different shapes of the calcium fragments and

the presence of anatomical structures next to the calcium-like deposits decreased the cross-correlation index and increased the difficulty to determine a cross-correlation cut-off (for determining whether there is a deposit or not). However, ROC analysis was used to determine the optimum cut-off and also the sensitivity and specificity. The experiments performed in this chapter were used to identify and address some challenges (high-pass filtering, deposit shape, and anatomical structures in tissue) present when detecting calcium deposits in tissue *via* cross-correlation in practice.

CHAPTER V

ESTIMATING THE CLINICAL VALUE OF

DETECTING MICROCALCIFICATIONS IN BREAST MRI *VIA* CROSS-CORRELATION

Introduction

In the previous chapters, the detection of calcium deposits in MR imaging *via* cross-correlation was implemented and the method's responses to different MR parameters (SNR, *TE*, and spatial resolution), deposit characteristics (size and position within a voxel), and image post-processing (filtering) methods were measured and validated. These findings were used to determine the optimum conditions (SNR, *TE*, spatial resolution, filtering) for the method to detect deposits of specific sizes. In MR images acquired with these optimum conditions, calcium fragments (< 1 mm) within gel and 1 mm calcium-like deposits within chicken breast tissue were detected *via* cross-correlation. In addition, receiver operator characteristic (ROC) analysis was applied to determine the cross-correlation cut-off needed to maximize sensitivity and/or specificity. In this chapter, we implemented and evaluated the cross-correlation method to detect simulated (realistic) microcalcifications in breast MR images at 7T in a preliminary effort to estimate the clinical value of the method.

Implementing microcalcification detection in breast MRI at 7T *via* cross-correlation faces three immediate challenges. First, a large proportion of human breast is fat tissue (30); therefore breast MRI should be acquired with fat suppression. However, fat

suppression also alters the phase signature of the deposits and therefore hampers detection. Second, during breast MRI scan sessions, in order to obtain quality images, the subject has to remain immobile and this limits the scan length to 20 minutes; therefore the available MR parameters for gradient echo 3D (*TE*, spatial resolution, and SNR) are limited, making optimization of the method challenging. Third, it will be difficult to test the method in patients with a history of microcalcifications. Upon diagnosis of malignant calcifications, biopsies are performed and metallic markers are implanted in the biopsy sites. While it is safe to use the markers at 3T (31), the markers have not been tested at 7T, so these patients cannot be scanned at 7T.

Each of the three challenges was addressed. First, the effect of fat suppression on the method was measured by simulations and experimentally. A new set of templates, compensating for the effect, were generated. Second, keeping acquisition times within 20 minutes, we acquired breast MRI of healthy controls at 7T with different spatial resolutions, *TE*s, and SNRs, and determined the combinations that facilitated detection of microcalcifications. Third, we tested the method in breast MR images of healthy volunteers containing realistic, simulated microcalcifications, modeled from biopsy samples of malignant breast cancer and inserted *in silico* into the MR images. In addition, the clinical value of the MR method was estimated by comparing its sensitivity and specificity with that of mammography.

Fat suppression and phase signature of deposits

Fat suppression methods diminish the signal in regions with the same precession frequency of fat. When water and fat are placed in a static field B_0, their protons experience a slightly different precession rate due to their different molecular structure. Fat signal arises from lipid protons in compounds containing CH_2 and CH_3 while water signal arises from hydrogen protons in in H_2O. As a result of those differences, the signal from fat is shifted to a lower frequency so that the difference between their precession frequencies Δf_{fw} is given by

$$\Delta f_{fw} = \frac{-\sigma_{fw} \gamma B_0}{2\pi} , \qquad \text{(V-1)}$$

where σ_{fw} is the chemical shift between water and fat (3.35×10^{-6}) expressed as a fraction of B_0, and γ is the hydrogen proton gyromagnetic ratio (2.68×10^8 rad/s/Tesla). When $B_0 = 7$ T, fat suppression methods diminish the signal in regions with a precession frequency -1.0 kHz relative to the precession frequency of water protons.

A spherical calcium deposit within tissue induces a disturbance in B_0 with the shape of a dipole containing a wide range of ΔB shifts. In gradient echo MR images, these shifts produce a phase signature with a wide range of precession frequencies (relative to the precession frequency of water). Figures V-1 shows the simulated frequencies induced by a 1 mm spherical calcium deposit surrounded by tissue inside a magnetic field strength of 7T (simulation described in detail in Chapter III). The views are parallel (panel a) and perpendicular (panel c) to B_0 and the frequencies have a range of [-1.5, 1.5] kHz.

Frequencies with range of [-0.95, 1.05] kHz are shown in panels b and d, parallel and perpendicular to B_0, respectively. When fat suppression is used in conjunction with gradient echo, the signal in regions with frequency around -1 kHz will be diminished.
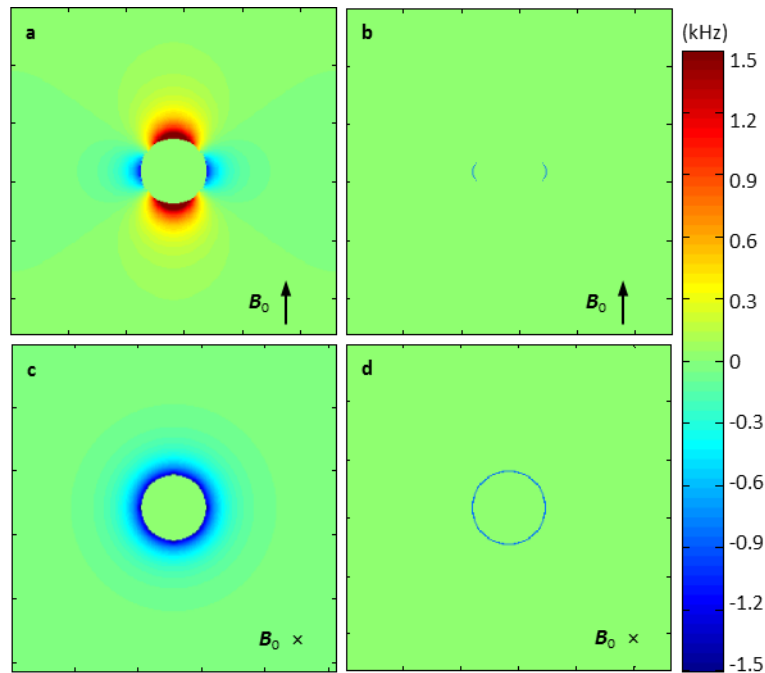
Figure V-1. Fat suppression effects on the phase signatures of deposits. Views parallel (panel a) and perpendicular (panel c) to B_0 of the simulated phase signature of a calcium deposit, where the suppressed region, around -1.0 kHz, is located in the negative lobe; for clarity, only the region between -0.95 and -1.05 kHz, is indicated in panels b and d, parallel and perpendicular to B_0, respectively.

MRI of calcium deposits using fat suppression

The effects of fat suppression on the phase signature of deposits were measured in MR images of a phantom containing calcium-like deposits, petroleum jelly, and water. Five 0.5 mm borosilicate glass beads (Aldrich, St. Louis, Missouri) were placed in a layer of petroleum jelly and then topped with distilled water. Water was used as a reference to verify that the water suppression method was working. The beads were chosen

because, like calcium deposits, they have very low water content and a magnetic susceptibility of $\chi = -11 \times 10^{-6}$ (9). Petroleum jelly was used because it contains a high concentration of lipids, and has the same magnetic susceptibility ($\chi = -9 \times 10^{-6}$) of water. The MR images were acquired using an Achieva 7.0T (Philips Medical Systems, Best, The Netherlands) with a local transmit/receive breast coil (32) for unilateral focused transmission/reception using two circular elements 15 cm in diameter, orthogonally aligned and driven in quadrature (33). A 3D gradient echo sequence with ProSet fat suppression (a selective excitation technique that employs a frequency and spatially selective excitation pulse) was used to obtain images sensitive to the phase signature of microcalcifications. The acquisition parameters were $TR/TE/\alpha$ = 12 ms/7.68 ms/10°, voxel size of (0.6 mm)^3, bandwidth = 531 Hz/pixel, FOV of 150 × 150 × 120, an acquisition matrix of 250 × 250 × 200, and acquisition time of 15 min. Images with and without fat suppression were acquired and the glass beads were detected *via* cross-correlation.

Breast MRI experiments

In order to perform detection of simulated microcalcifications in breast MRI *via* cross-correlation, breast MRI of healthy volunteers were acquired. MR images were acquired using the Achieva 7.0T with the local transmit/receive 15 cm breast coil described above. A 3D gradient echo sequence with ProSet fat suppression was used to obtain images. ProSet fat suppression was selected because it does not increase gradient echo acquisition time. We used two spatial resolutions (0.4 mm)^3 and (0.6

mm)^3 to determine the combination that facilitated detection. For the (0.4 mm)^3 data,

we employed $TR/TE/\alpha$ = 10 ms/6.9 ms/10°, bandwidth = 661 Hz/pixel, a FOV of 140 ×

140 × 80 mm, an acquisition matrix of 350 × 350 × 200 for an acquisition time of 12 min.

For the (0.6 mm)^3 data we employed $TR/TE/\alpha$ = 6.7 ms/3.0 ms/10°, BW = 531 Hz/pixel,

FOV of 150×150×120 mm, and an acquisition matrix of 250×250×200 for an acquisition

time of 7 min.

Extraction of microcalcification shapes from breast cancer samples

In order to simulate malignant microcalcifications in breast MR images, calcification

shapes were extracted from high resolution CT images of breast cancer biopsies. CT

images of breast cancer biopsy samples (labeled S1, S2, and S3) prepared in paraffin

blocks were acquired using a Scanco Medical microCT50 (Brüttisellen, Switzerland) with

the following parameters: tube voltage of 45 kVp, exposure time of 300 ms, anode

current of 200 μA, five hundred projections acquired over 180 degrees, and longitudinal

resolution of 7.5 μm. 2D images were reconstructed from the projections. Then multiple

images from adjacent slices were used to reconstruct a three-dimensional volume with

isotropic voxel size of (7.5 μm)^3. Calcium, tissue, and background paraffin appeared with

different signal intensities, so a threshold based segmentation was applied to separate

calcium from tissue and paraffin and to generate a binary image containing only

calcium. The Matlab function 'BWCONNCOMP' was applied to the binary image to

identify all of the connected components, their locations, dimensions (length, width,

and height), and shapes. Components with dimensions > 0.1 mm surrounded by tissue were classified as microcalcifications and their shapes were recorded.

Detection of simulated microcalcification in breast MRI via cross-correlation

Phase signatures of microcalcifications were inserted *in silico* into breast MR images from healthy volunteers and detected *via* cross-correlation method. The phase signatures of the microcalcifications were simulated using the method described in Chapter III and the microcalcification shapes extracted from the breast cancer samples. The signatures were inserted *in silico* into the breast MR images by adding their phase to the argument of the MR complex images. Individual and clusters of microcalcifications with sizes between 0.4 mm and 1.0 mm were inserted in four different locations within glandular tissue in each set of breast MR images, one with voxel size of $(0.4 \text{ mm})^3$ and the other with voxel size of $(0.6 \text{ mm})^3$. In order to consider partial volume effects, each microcalcification was systematically moved within the voxel in four equally spaced locations on each dimension, totaling 64 different locations. Cross-correlation analysis was applied to breast MRI data to detect the microcalcifications.

Clinical value of detection of microcalcifications in breast via cross-correlation

The clinical value of cross-correlation method was estimated by comparing the sensitivity and specificity of the method for detecting simulated microcalcifications in breast with those of mammography. ROC analysis was applied to the CCMVs obtained

when detecting the simulated microcalcifications in the aforementioned section to determine the sensitivity and specificity.

Results

Fat suppression effects on cross-correlation

The effects of fat suppression on the phase signature of deposits were measured in gradient echo images of a phantom containing petroleum jelly, water, and calcium-like deposits. Figure V-2 shows the magnitude images of the phantom. Panel a displays the magnitude image acquired without fat suppression where the fat (petroleum jelly) is indicated by the arrow. Panel c deptcts the same image acquired with fat suppression that caused a reduction in the signal intensity of the petroleum jelly. Panel b shows the magnified view of the phase signature of a calcium-like deposit, indicated by the green insets, acquired without fat suppression; the signature has a dipole shape with positive lobes parallel to B_0 and negative lobes perpendicular to B_0. Panel d displays the same phase image acquired with fat suppression which caused a reduction in signal intensity on the negative lobe, indicated by a white arrow. Fat suppression had different effects on the magnitude and phase images of calcium deposits. In the magnitude images, fat suppression reduced the signal intensity of petroleum jelly, and in the phase images, it reduced the signal from the negative lobe of the phase signature of the deposit. The location of the regions affected is the same as suggested by simulations in Figure V-1.

In order to compensate for the fat suppression effects in the cross-correlation method at 7T, the library of templates was modified. In the templates, the signal in regions with frequencies between -0.9 and -1.10 kHz was reduced to 10% of its original value.
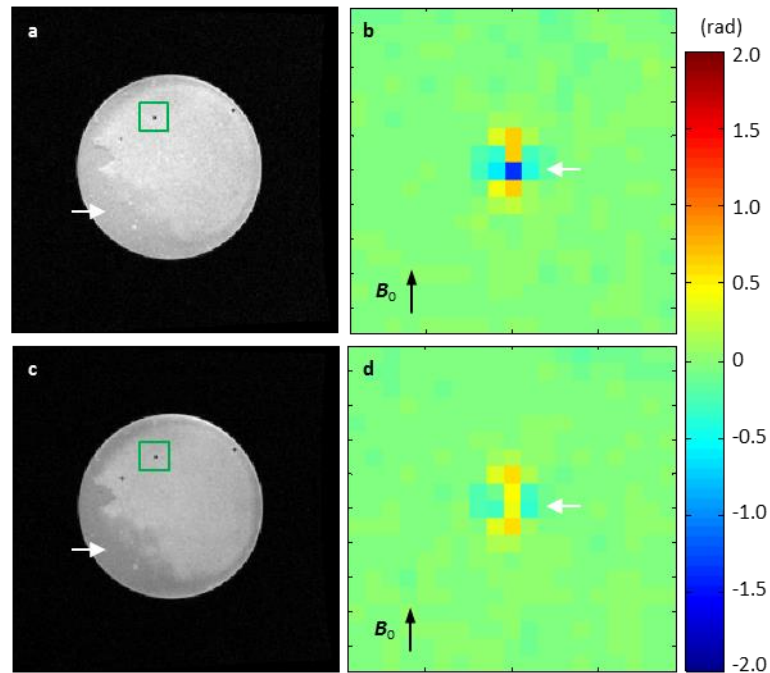
Figure V-2. Fat suppression effects in gradient echo images of a phantom containing calcium-like deposits, water, and lipids. Panel a shows the magnitude acquired without fat suppression where the fat is indicated by the arrow. Panel c displays the same image acquired with fat suppression that caused a reduction in the signal intensity of the petroleum jelly. Panel b shows the magnified view of the phase signature of a calcium-like deposit, indicated by the green inset in the magnitude images, acquired without fat suppression. Panel d displays the same phase image acquired with fat suppression, which caused a reduction in the signal intensity on the negative lobe, indicated by the withe arrow.

Extraction of microcalcification shapes from breast cancer samples

Central to the simulations is the extraction of microcalcification shapes from high resolution CT images of breast cancer samples. Figure V-3 shows images of the breast

cancer sample S1. Panel a shows the photograph of the sample prepared in paraffin block and panel b shows the corresponding high resolution CT image. The sample contained microcalcifications that were visible in the CT image, indicated by white arrows in the magnified view of the green inset in panel c.
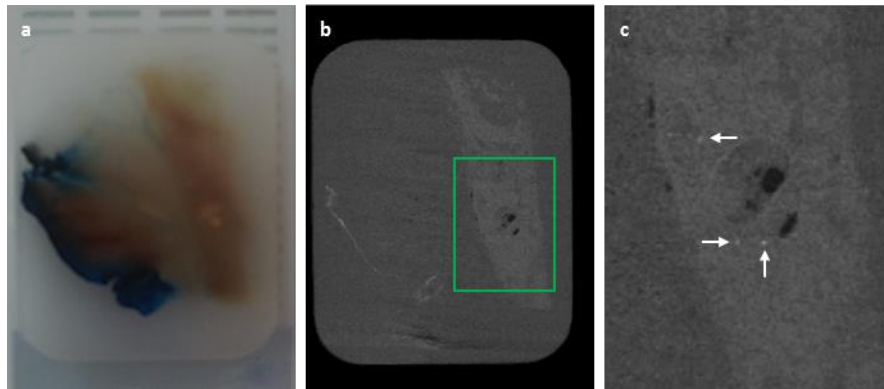
Figure V-3. Breast cancer biopsy. Photograph of breast cancer sample S1 (panel a), prepared in paraffin block, and corresponding high resolution CT image (panel b); the magnified view of the inset (panel c) shows microcalcifications, indicated by white arrows.

Figure V-4 illustrates the shape extraction of one microcalcification. Panel a shows the high resolution CT image of breast cancer biopsy S2 containing a microcalcification in the green inset. Panel b depicts the magnified view of the inset; threshold based segmentation was applied to this image to separate calcium from tissue and background and to generate a binary image containing the shape of the microcalcification (panel c). The shape of the microcalcification was obtained from the binary image using the Matlab function 'BWCONNCOMP'. Panel d shows the 3D view of the shape.
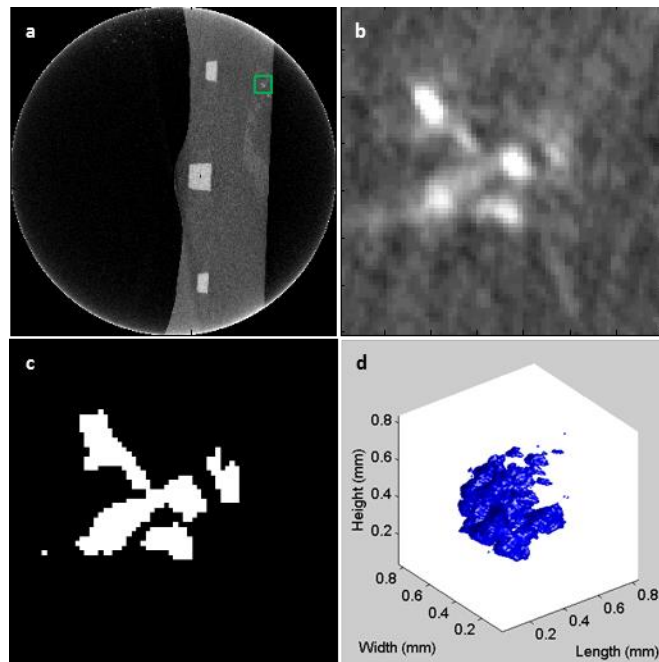
Figure V-4. Measurement of microcalcification shape from breast cancer biopsy block. The high resolution CT image of breast cancer biopsy (panel a) shows a microcalcification (green inset) depicted in more detail in a magnified view (panel b). Threshold based segmentation applied to this image separated calcium from tissue and background and generated a binary image containing the shape of the microcalcification (panel c); a 3D view of the shape is depicted in panel d.

Detection of simulated microcalcifications in breast MRI

Simulated microcalcifications were inserted *in silico* into breast MRI of healthy controls and detected *via* cross-correlation. Figure V-5 illustrates the insertion and detection of four microcalcifications. Panel a shows the magnitude image of a healthy control acquired with voxel size of $(0.6 \text{ mm})^3$. Panel b depicts a magnified view of the location of the insertion, indicated by the white inset in the magnitude image; the insertions were made within glandular tissue, at the locations indicated by white arrows. Panel c displays the shape of the microcalcification used to simulate the phase signature and its dimensions, $0.64 \times 0.71 \times 1.065$ (mm^3). Panel d depicts the phase image

69
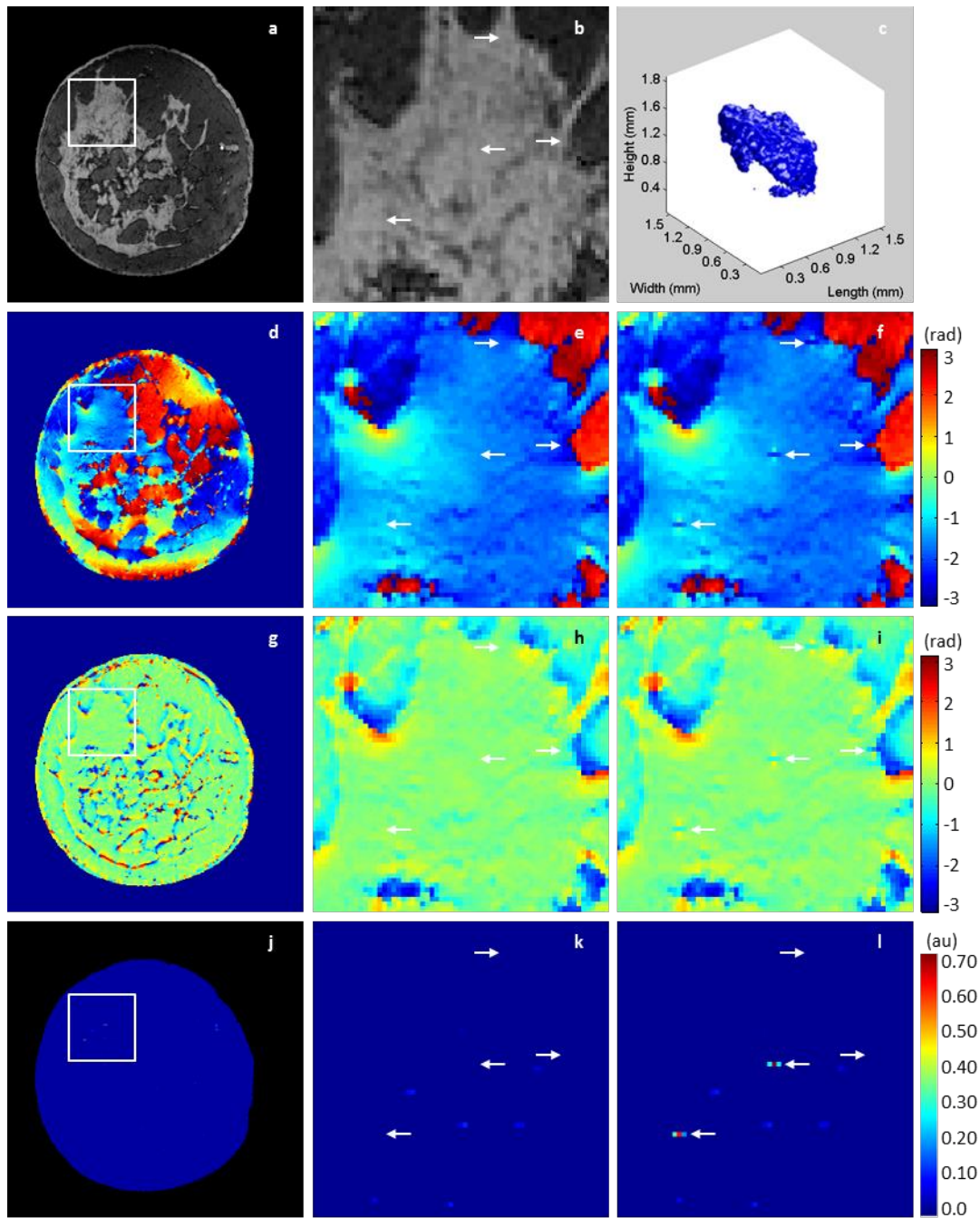
Figure V-5. Detection of simulated microcalcification in breast MRI *via* cross-correlation. The insertions where made within the fibroglandular tissue, indicated by the high intensity regions in the magnitude image (a); the exact locations are indicated by the arrows in the inset (panel b). Panel c shows the shape of the microcalcification. Panels d-f depict the phase image before filtering and panels g-h after filtering; panels j-l display the similarity matrix. Panels e,h, and k depict the images before insertion and panels f, i, and l after insertion.
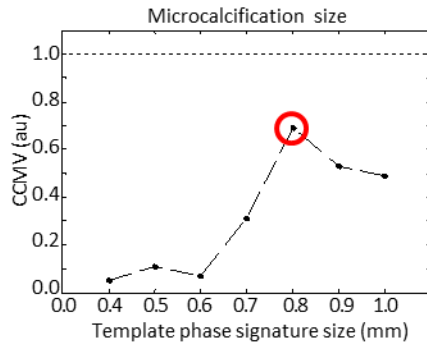
Figure V-6. Detection of simulated microcalcification size in breast MRI *via* cross-correlation. The size of the microcalcification is determined in the plot of CCMVs obtained from the phase image and templates generated with deposit sizes between 0.4 mm - 1.0 mm. The estimated size of 0.8 mm of the detected deposit is indicated by the maximum CCMV across the templates and the uncertainty by the difference between phase signature sizes in the library. In this case, it is ±0.05 mm.

of the healthy control before high-pass frequency filtering, panel e shows the corresponding magnified view before the *in silico* insertion of the microcalcification phase signature, which creates a small change in phase and panel f shows the same magnified view after the insertions. Panel g depicts the phase image from the healthy control after filtering, panel h displays the corresponding magnified view before the insertions and panel i after the insertions. Panel j displays the cross-correlation matrix obtained from a template generated with a deposit size of 0.8 mm and the phase image (panel g) after the insertions. Panel k shows the magnified view of the similarity matrix before the insertions and panel l shows the magnified view after the insertions. Simulated microcalcifications far from fat and fibroglandular tissue borders where detected (lower arrows panel l) with a CCMV of 0.68; before insertion the cross-correlation index was 0.16. Simulated microcalcifications next to the boundary (upper

71

arrows) were not detected. The size of the microcalcification was determined from the plot of CCMVs obtained between the phase image and the library of templates generated with deposit sizes between 0.4 – 1.0 mm. Figure V-6 shows the CCMV plot where the maximum CCMV across the templates indicates the size of the deposit, in this case 0.8 mm, and the uncertainty is indicated by the difference between phase signature sizes in the library, in this case, ±0.05 mm.

Sensitivity and specificity of cross-correlation for detecting

simulated microcalcifications in breast MRI

In order to estimate the clinical value of cross-correlation, ROC analysis was applied to the detection of simulated calcifications in breast MR *via* cross-correlation and the sensitivity and specificity of the method were measured. Figure V-7 sows the ROC curve for detection of 0.8 mm microcalcifications in images with voxel size of $(0.4 \text{ mm})^3$ (panel a) with sensitivity of 75%, specificity of 75%, and AUC of 0.89; and the detection of 1.0 mm microcalcifications in images with voxel size of $(0.6 \text{ mm})^3$ (panel b) with sensitivity of 78%, specificity of 87%, and AUC of 0.90. The AUCs indicate moderate sensitivity of 78%, specificity of 87%, and AUC of 0.90. The AUCs indicate moderate discriminatory power for large microcalcifications. (Recall that an AUC = 0.5 is chance.) However, smaller deposits are detected with less sensitivity and specificity.

72
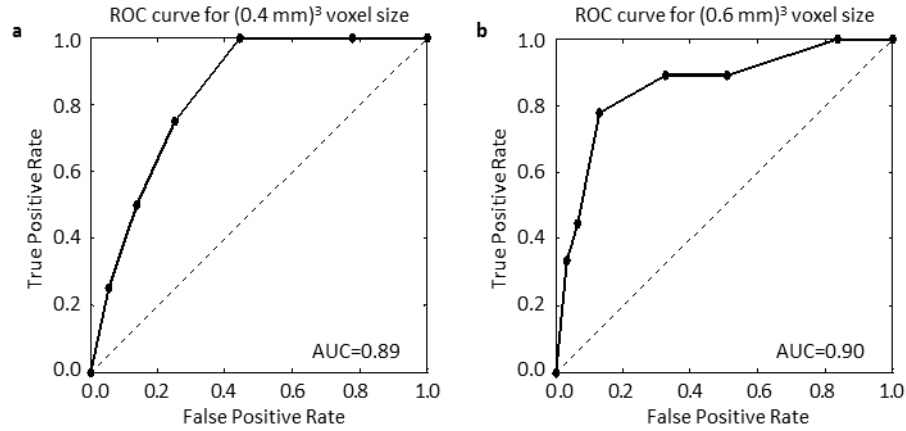
Figure V-7. ROC curve analysis of detection of simulated microcalcifications in breast MRI *via* cross-correlation. ROC curve for detection of 0.8 mm microcalcifications in MR images with voxel size of $(0.4 \text{ mm})^3$ (panel a) and 1.0 mm microcalcifications in images with voxel size of $(0.6 \text{ mm})^3$ (panel b).

Table V-1 presents the sensitivity, specificity, and AUC obtained when ROC analysis was applied to the detection of microcalcifications with sizes between 0.4 and 1.0 in steps of 0.1 mm in images with voxel sizes of $(0.4 \text{ mm})^3$ and $(0.6 \text{ mm})^3$. The method, in general, detected larger microcalcifications better than the smaller ones; this is indicated by the increase of sensitivity, specificity, and AUC with deposit size.

Table V-1 ROC analysis of detection of simulated microcalcifications in breast MRI *via* the cross-correlation method		
	Sensitivity, specificity, AUC	
Deposit size (mm)	Image voxel size $(\text{mm})^3$	
	0.4	0.6
0.4	75, 19, 0.42	43, 32, 0.45
0.5	50, 50, 0.61	33, 41, 0.48
0.6	87, 54, 0.80	78, 47, 0.65
0.7	87, 54, 0.80	56, 44, 0.56
0.8	75, 75, 0.89	78, 66, 0.80
0.9	75, 52, 0.76	78, 66, 0.80
1.0	87, 54, 0.81	78, 87, 0.90

Estimating the clinical value of the cross-correlation method

The results summarized in Table V-1 suggest that microcalcifications with sizes between 0.4 - 1.0 mm in images with voxel sizes of $(0.4 \text{ mm})^3$ and $(0.6 \text{ mm})^3$ can be detected in breast MRI at 7T with sensitivity between 50%-75% and specificity between 16%-87%. Since mammography has far superior sensitivity (74%-95%) and specificity (89%-99%), the clinical value of detection of microcalcifications *via* cross-correlation method is currently limited compared to that of mammography.

Discussion

Detection of microcalcifications in breast MRI at 7T *via* cross-correlation is limited by the available MR parameters for gradient echo 3D sequence (*TE*, spatial resolution, and SNR). In Chapter I, the *TE*s needed to detect deposits of various sizes in images with different spatial resolutions were computed and summarized in Table III-1; however, not all of these values were practical. Only spatial resolutions of $(0.4 \text{ mm})^3$ and $(0.6 \text{ mm})^3$ and their corresponding *TE*s of 6.9 ms and 3.0 ms, respectively, were feasible. Smaller *TE* values were not available for these voxel sizes, and larger *TE* values produced images with very low SNR and increased the acquisition time. According to Table III-1, only microcalcifications with sizes of approximately 0.5 mm should be detected in images acquired with voxel sizes of $(0.4 \text{ mm})^3$, and only microcalcifications with sizes of approximately 0.8 mm will be detected in images acquired with voxel sizes of $(0.6 \text{ mm})^3$. Detection of simulated microcalcifications in images acquired with these two MR parameter sets agrees with the sizes suggested by simulation (see Table V-1). In images

acquired with a voxel size of (0.4 mm)^3, microcalcifications with sizes 0.6, 0.7, and 0.8 mm are detected with the best sensitivity and specificity. Similarly, in images acquired with voxel size of (0.6 mm)^3, microcalcifications with sizes 0.8, 0.9 and 1.0 mm are detected with the best sensitivity and specificity. All this indicates that detection of microcalcifications in breast MRI at 7T is limited by the available *TE*'s and spatial resolution of images (acquired in less than 20 minutes).

ROC analysis indicted that cross-correlation method detected 0.8 mm simulated microcalcifications in images with voxel size of (0.4 mm)^3 with an AUC =0.89 and 1.0 mm simulated microcalcifications in images with voxel size of (0.6 mm)^3 with an AUC =0.90 (See Figure V-6) therefore the method is promising for detecting large calcium deposits in breast MRI at 7T; we hypothesize that the MR methods of compressed sensing (CS) may be able to improve the detection of smaller calcium deposits *via* cross-correlation. According to simulations performed in Chapter III, calcium deposits with size of 0.3 mm should be detected on gradient echo 3D images with voxel size of (0.2 mm)^3, assuming a *TE*=3.72 is available (see Table III-1); however these data will take longer than 20 minutes to acquire. CS can, in principle, dramatically improve spatial resolution with no extra increase in time (34) therefore making feasible to obtain gradient echo 3D images with voxel size of (0.2 mm)^3 and allow detection *via* cross-correlation.

We found that fat suppression, besides decreasing the magnitude of signal coming from fat, also has a deleterious effect in detecting calcium deposits *via* cross-correlation; fat suppression reduces the signal intensity in some regions within the negative lobe of the phase signature of deposits (see Figures V-1 and V-2). This change in the phase

signature causes a reduction in CCMV making detection more challenging. In order to compensate for the fat suppression effects, the library of templates was modified. In the templates, the signal in regions with frequencies between -0.9 and -1.10 kHz was reduced to 10% of its original value. We believe that this new library will account for the decrease on CCMV. However, more experiments are needed to quantify the effect of fat suppression.

CHAPTER VI

CONCLUSION

We have evaluated a new MRI-based method for detecting calcium deposits, using their characteristic susceptibility effects in practical conditions to provide insight into its clinical value for detecting breast microcalcifications at high field (7T). Unlike X-ray mammography, which is currently the gold standard, this alternative MRI method does not expose breasts to ionizing radiation and is not affected by breast density. The method was optimized to detect calcifications associated with malignancy as classified by the BI-RADS; specifically, microcalcifications that are < 1.0 mm, punctate, clustered, and pleomorphic in shape (1). The method was designed to detect the characteristic, unique dipole signatures of calcium deposits in phase images *via* cross-correlation between the images and a library of templates containing simulated phase signatures of deposits. The influences of the SNR and various MR parameters on the method were determined using simulations and validated in experiments with phantoms. The method was optimized for detecting calcium fragments within gel, calcium-like objects within chicken breast tissue, and , importantly, simulated microcalcifications, modeled from biopsy samples of malignant breast cancer, inserted *in silico* into breast MRIs of healthy controls. Receiver operator characteristic (ROC) curve analysis was applied to the method to determine the cross-correlation index cutoff (for deciding whether there is a deposit or not), sensitivity, specificity, and area under the curve (AUC).

The influences of deposit position, SNR, spatial resolution, high-pass filtering, and fat suppression on the method were determined and used to optimize detection at 7T field strength of 1 mm calcium-like deposits, calcium fragments with sizes of 0.14 – 0.79 mm, and simulated microcalcifications (0.4 – 1.0 mm) in images with voxel sizes between (0.2 mm)^3 and (0.6 mm)^3. In images acquired using the 7T clinical scanner with acquisition times under 12 minutes, simulated microcalcifications 0.6 – 1.0 mm in size were detected in images with voxel sizes of (0.4 mm)^3 and (0.6 mm)^3 with sensitivity, specificity, and AUC of 75 – 87%, 54 – 87%, and 0.76 – 0.90, respectively. In images acquired with the small animal 7T scanner, smaller calcium fragments (0.3 – 0.4 mm) were detected in images with voxel sizes of (0.2 mm)^3 and (0.4 mm)^3 with sensitivity, specificity, and AUC of 78 – 90%, 51 – 68%, and 0.77 – 0.88, respectively. Thus the method detected the deposits with high sensitivity and moderate specificity. This is consistent with the findings in simulations: since the method can detect deposits with different shapes with similar CCMVs, the method has intrinsic high sensitivity and low specificity. Sensitivity and specificity depended directly on the CCMV cut-off (used to determine if a deposit was present or not), which can be chosen to obtain different combinations of sensitivity and specificity (see Figure IV-5); therefore it is difficult to evaluate the method using sensitivity and specificity alone. A more appropriate indicator of the method's performance is the AUC obtained from ROC analysis. The AUC results indicate the method is promising for larger calcification and therefore warrants further investigation.

For the eventual application of breast calcification detection in patients, the method needs to be further refined and optimized. In clinical settings the method is promising for detecting large microcalcifications with a size range of 0.6 − 1.0 mm within the breast at 7T; however, microcalcifications associated with malignancy can be below 0.6 mm, so the ability to detect these smaller sizes is important. Detection of smaller deposits may be possible in images with higher spatial resolution. Results indicate that in order to detect calcium fragments with sizes under 0.6 mm, we need images with isotropic voxel sizes of $(0.2 \text{ mm})^3$ (see Table IV-1). Unfortunately, because images of sufficient SNR take too long to acquire using current MR methods, it is clinically impractical. Compressed sensing (CS) can, in principle, dramatically improve spatial resolution with no increase in acquisition time thereby potentially allowing detection of smaller deposits. Another strategy to reduce acquisition time is to implement multiple coils arrays, which can reduce the number of phase encoding steps.

For preclinical research applications, the method can be implemented at higher magnetic fields yielding many advantages. The phase signature of a deposit depends on the product of B_0 and TE; if we increase B_0, shorter TEs can be used. Shorter TEs allow the use of smaller TRs and, therefore, a reduction in acquisition times. Also, with increased B_0 the gain in SNR can be used to obtain higher spatial resolution and, therefore, detect smaller deposits.

Our results indicate that the method is promising for detecting macro and microcalcifications within tissue using small animal scanners as well as in clinical MRI. For small animal scans the small field of view (FOV) allows for reduced acquisition times;

in addition, the scan time can be lengthened to facilitate the acquisition of gradient echo images with higher spatial resolutions from different parts of the sample. Therefore, the method can be implemented to detect smaller calcium deposits, such as those in xenograft tumors, renal calcium deposits, or calcified lesions in brain. In addition, the method can be easily adjusted to detect paramagnetic objects such as iron particles or blood, making the method attractive for detection of hemorrhage or iron particles within tissue. For clinical applications outside of breast microcalcification detection possible regions of interest include the kidney or brain; however, they require larger FOVs, such that gradient echo images will take longer to acquire, which makes the method challenging to apply for larger areas of the body. Therefore, clinically, the method is the most promising for breast calcification detection.

APENDIX A

GRADIENT ECHO SIMULATIONS

This appendix contains a detailed description of the computations and programs used during the gradient echo simulations performed in this dissertation. In addition to the step-by-step description of the computations, a flow-chart and the commented code have been added to illustrate the simulation process.

The core of the simulations is the pivotal function `sim_image`; this function takes the discrete version of the calcium deposit and generates the magnitude and phase gradient echo images for specific conditions of *TE*, location of the deposit within the voxel, SNR, and spatial resolution. `sim_image` is used in combination with more elemental scripts to compute the template libraries, *TE* needed to constrain the phase signature within [-π, π], etc. Below is a description of the function `sim_image`.

`sim_image` input parameters are MAT, *TE*, SNR, offset, deposit size, and spatial resolution. Their relationships are described below:

- MAT is a binary matrix with the discrete version of the deposit. Ones represent calcium and zeros water. Its size depends on the deposit size *D* and the image spatial resolution *s*, and the field of view fov. Deposits were discretized using "element voxels" with isotropic size of *D*/30 (see Figure III-1). The field of view was set depending on the deposit size and the spatial resolution. For deposits smaller than the spatial resolution, the field

of view was set to 9s because we needed at least 9 image voxels to generate the phase signature of the deposit. For deposits larger than the spatial resolution, the field of view was set to 5D.

- *TE*, SNR, offset, deposit size, and spatial resolution are parameters that required no further computation. Offset is a three element matrix indicting the position location of the deposit in mm with respect to the center of the voxel.

`sim_image` contains the physical values for proton density, ρ, the longitudinal and transverse relaxation times, T_1 and T_2, respectively, and the magnetic susceptibility, χ, all appropriate for B_0=7T. Element voxels within water were set to the susceptibility of tissue water and the relaxation time constants of glandular breast tissue water at 7T, and spin density of 1×10^6 arbitrary units. Element voxels within calcium were set to susceptibility of calcium but with spin density of zero and no relaxation times; therefore magnitude and phase were not computed inside the deposit. However, its susceptibility created phase disturbances surrounding the deposit.

The computation order and the subordinated functions in `sim_image` are illustrated in Figure A-1. `sim_image` takes a 3D binary matrix containing the binary digital description of the deposit. Two sets of simulation matrices are formed using the binary matrix: the susceptibility matrix and a matrix containing the MR properties of the deposit. Both matrices have the same dimensions as the original binary matrix. The susceptibility matrix is used by the function `bshift_sal` to compute the phase of the gradient echo signal using the Salomir transformation (26) and the parameters *TE*, and

B_0. The magnitude of the gradient echo signal is computed by applying the gradient echo equation to the image matrix containing the MR properties of the deposit and the parameters *TE*, *TR*, and B_0. The complex signal matrix is formed using the magnitude and phase matrices. At this point noise is added using the function `sim_snr`. The final image is formed by the function `cambiate` which computes a vectorial sum of elements from the complex signal matrix to obtain image voxels. The resulting image is complex and smaller than the simulation matrix size.

Gadient Echo simulaton
function: sim_image

```
Calcium and water
binary image
```

```
Image with T_1, T_2, and ρ
properties
of water
```

```
Susceptibility image of
calcium and water
χ properties
```

```
Magnitude computation
Grad echo Eq, TE, B_0, TR
```

```
Phase computation
Salomir Transf, TE, B_0, and
function: bsift_sal
```

```
Complex image
formation
```

```
Noise addition
function: sim_snr
```

```
Image voxels
computation
function: cambiate
```
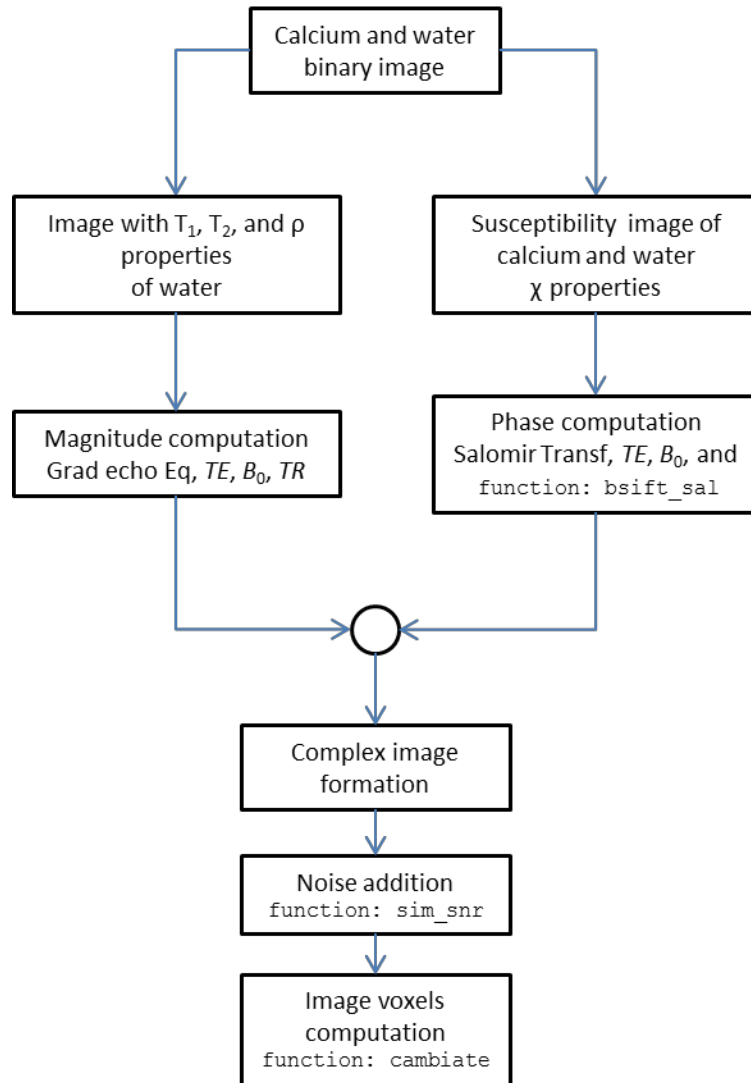
Figure A-1. Flow chart of the gradient echo simulation function `sim_image`. Element voxels within water were set to the susceptibility of tissue water and the relaxation time constants of glandular breast tissue water at 7T, and spin density of 1×10^6 arbitrary units. Element voxels within calcium were set to susceptibility of calcium but with spin density of zero and no relaxation times; therefore magnitude and phase were not computed inside the deposit. However, its susceptibility created phase disturbances surrounding the deposit.

MATLAB code

```matlab
function [Mxy_ini IMG_S_CPLX]=sim_image(DEP_SIZE,MAT, FOV, OFFSET, TE,win_size,
snr_ad)
% This script simulates the Gradient echo image for a calcium deposit where:
%
%   DEP_SIZE is the diameter of the spherical deposit
%   MAT is the matrix containing the dimensions i.e. [280 280 280]
%   FOV is the matrix containing the field of view
%   OFFSET is the matrix containing the offset of the deposit within the
%           center of the voxel
%   TE is the echo time (s)
%   win_size is the number of element voxels per image voxel
%   Mxy_ini is the inital signal intensity of transversal vector
%   IMG_SMALLER_CPLX is the simulated image (complex)
%
%%%%%%%
%
%
%%%%%%%%%% MR Parameters
%
% Calcium
T1C=0; %(s)
T2SC=0; %(s)
MC=0; %(a.u.)
XC=-11e-6; % SI dimensionless units
% Water
T1W=1.622; %(s)
T2SW=0.064; %(s)
MW=1e6; %(a.u.) KF=0.0881, if we want 1 use y*KF=1
XW=-9e-6; % SI dimensionless units
%%%%%%%%%% Gradient echo parameters
```

85

```matlab
B0=7; %(T)

gam = 2.675e8;

TR= 1.500; %(s)

FA_RAD=acos(exp(-TR/T1W)); % computed using Ernst angle Eq.

FA=FA_RAD*360/(2*pi);

% inital signal intensity of transversal vector

E1_W=exp(-TR/T1W);

E2_W=1;

Mxy_ini=MW*sind(FA)*(1-E1_W)/(1-cosd(FA)*E1_W);

%%%%%%%%%%%%%

% spherical calcium model (index indicates location of calcium

[idx] = draw_sphere(DEP_SIZE/2, MAT, FOV, OFFSET);

%%%%%%%%   Magnitude

E2=single(zeros(MAT)*0+T2SW);

E2(idx)=T2SC;

E2=exp(-TE./E2);

E1=single(zeros(MAT)*0+T1W);

E1(idx)=T1C;

E1=exp(-TR./E1);

MAG=single(zeros(MAT)*0+MW);

MAG(idx)=MC;

MAG=(MAG*sind(FA)).*(1-E1).*E2./(1-cosd(FA)*E1);

clear E1 E2

%%%%%%%%   Phase

PHA = bshift_sal(idx,MAT, XW, XC, B0);

PHA=gam*TE*PHA; % TE in seconds here...

%%%%%%%%   Complex image

IMG_CPLX=MAG.*exp(i*PHA);

[IMG_NOISY]=sim_snr(IMG_CPLX,snr_ad); % add some noise...

IMG_CPLX=IMG_NOISY;

clear PHA MAG

IMG_S_CPLX=cambiate(IMG_CPLX,win_size);
```

86

```matlab
function [idx] = draw_sphere(a, N, L, c);
% This script discretize the spherical model
% a is the radius of the deposit
% N is a three element matrix containing the size of the simulated matrix
% L is a three element matrix containing the size of the FOV (in mm)
% c is a three element matrix containing the offset of the object (within
% the center of the matrix)
% idx contains a pointer to the voxel elements containing calcium
res=L./N;
xnd=-N(1)/2*res(1)+res(1)/2-c(1):res(1):N(1)/2*res(1)-res(1)/2-c(1);
znd=-N(2)/2*res(2)+res(2)/2-c(2):res(2):N(2)/2*res(2)-res(2)/2-c(2);
ynd=-N(3)/2*res(3)+res(3)/2-c(3):res(3):N(3)/2*res(3)-res(3)/2-c(3);
xnd=single(xnd);
znd=single(znd);
ynd=single(ynd);
[X Z Y]=meshgrid(xnd,znd,ynd);
Z=(Z*(-1));
X=(X*(-1));
Y=(Y*(-1));
idx = single(find((X.^2+Y.^2+Z.^2)<a^2));


function [IMG_SMALLER]  =cambiate(IMAGE, N);
% This script averages elements of a matrix into a smaller matrix
% IMAGE is the original matrix
% N is the window size on which M will be divided into
% IMG_SMALLER is the resulting matrix
%
dim=size(IMAGE);
R=floor(dim./N);
IMG_SMALLER=zeros(R(1),R(2),R(3));
for l=1:R(1)
```

```matlab
    for m=1:R(2)

        for p=1:R(3)

            T=IMAGE(((l-1)*N(1)+1):l*N(1),((m-1)*N(2)+1):m*N(2),...

                ((p-1)*N(3)+1):p*N(3));

            IMG_SMALLER(l,m,p)=mean(T(:));

        end

    end

end


function B0_shift=bshift_sal(idx_calcium,MAT, XW, XC, B0)
% This function computes the B0_shift using the Salomir transformation
% idx_calcium indicates element voxels with calcium (0 indicates water)
% constants in units as follows
%   MAT is the element matrix size
%   XW=-9e-6; Mag susceptibility of water (SI dimensionless units)
%   XC=-11e-6; Mag susceptibility of calcium (SI dimensionless units)
%   B0=7;  Static magnetic field (Tesla)
% compute  dipole
ind=[MAT MAT MAT];

sz = ind(1);

sx = ind(2);

sy = ind(3);

%obtain denominator
kx = [-sx/2:1:(sx/2-1)];

ky = [-sy/2:1:(sy/2-1)];

kz = [-sz/2:1:(sz/2-1)];

kx = single(kx);

ky = single(ky);

kz = single(kz);

%according to coordinate of ref [Z X Y] therefore Kz is Kx3D
[kx3D,kz3D,ky3D] = meshgrid(kx,kz,ky);

kx3D=(kx3D*(-1));
```

```matlab
kz3D=(kz3D*(-1));

ky3D=(ky3D*(-1));

Ksquared = kx3D.^2 + ky3D.^2 + kz3D.^2;

clear kx3D ky3D

numeratore =(1/3 - kz3D.^2 ./ Ksquared );

clear Ksquared kz3D

idx = (find(isnan(abs(numeratore))));

numeratore(idx)=0;

B0_shift=numeratore*0+XW;

% compute Fourier 3D of susceptibility bulk

B0_shift(idx_calcium)=XC;

B0_shift=(fftshift(fftn(B0_shift)));

B0_shift=B0_shift.*numeratore;

clear numeratore

B0_shift =-B0*(ifftn(fftshift(B0_shift)));

B0_shift(idx_calcium)=0;


function [IMG_RES]  =sim_snr(IMG_ORG,SNR_desired);

% IMG_ORG must be complex

ind=size(IMG_ORG);

sz = ind(1); sx = ind(2); sy = ind(3);

% background

IMG_CPLX=zeros(sz,sx,(sy+4));

IMG_CPLX(:,:,(sy+1):(sy+4))=1;

idx_noise = find(IMG_CPLX==1);

% signal

IMG_CPLX=IMG_CPLX*0;

IMG_CPLX(1,:,1:sy)=1;

IMG_CPLX(sz,:,1:sy)=1;

IMG_CPLX(:,1,1:sy)=1;

IMG_CPLX(:,sx,1:sy)=1;

IMG_CPLX(:,:,1)=1;
```

```matlab
IMG_CPLX(:,:,sy)=1;

idx_signal = find(IMG_CPLX==1);

IMG_CPLX=IMG_CPLX*0;

IMG_CPLX(:,:,1:sy)=IMG_ORG(:,:,:);

RandStream.setDefaultStream(RandStream('mt19937ar','seed',sum(100*clock)));

RE_NOISE=random('Normal',0,1,sz,sx,(sy+4));

IM_NOISE=random('Normal',0,1,sz,sx,(sy+4));

NOISE_FACTOR=(3e6)/SNR_desired;

IMG_RE=real(IMG_CPLX)+NOISE_FACTOR*RE_NOISE;

IMG_IM=imag(IMG_CPLX)+NOISE_FACTOR*IM_NOISE;

IMG_ABS=abs(IMG_RE+IMG_IM*i);

signal_mean=mean(IMG_ABS(idx_signal));

noise_std=std(IMG_ABS(idx_noise));

if noise_std<1e-4

    SNR=1000000;

else

SNR=sqrt(2-pi/2)*signal_mean/noise_std;

end

dSNR=(SNR-SNR_desired);

while abs(dSNR) > .25

    if SNR>=SNR_desired

        %NOISE_FACTOR=NOISE_FACTOR+(exp(-SNR/500));

        NOISE_FACTOR=NOISE_FACTOR+abs(dSNR);

        %NOISE_FACTOR=NOISE_FACTOR+0.0001;

    end

    if SNR<SNR_desired

        %NOISE_FACTOR=NOISE_FACTOR-(exp(-SNR/500));

        NOISE_FACTOR=NOISE_FACTOR-abs(dSNR);

        %NOISE_FACTOR=NOISE_FACTOR-0.0001;

    end

    IMG_RE=real(IMG_CPLX)+NOISE_FACTOR*RE_NOISE;

    IMG_IM=imag(IMG_CPLX)+NOISE_FACTOR*IM_NOISE;;
```

```matlab
IMG_ABS=abs(IMG_RE+IMG_IM*i);

signal_mean=mean(IMG_ABS(idx_signal));

noise_std=std(IMG_ABS(idx_noise));

if noise_std<1e-4

    SNR=1000000;

else

SNR=sqrt(2-pi/2)*signal_mean/noise_std;

end

    disp(SNR)

    dSNR=(SNR-SNR_desired);

end

IMG_CPLX_NOISY=IMG_RE+IMG_IM*i;

IMG_RES=IMG_ORG*0;

IMG_RES(:,:,:)=IMG_CPLX_NOISY(:,:,1:sy);
```

REFERENCES

1. D'Orsi CJ, Mendelson EB, Ikeda DM, et al 2003. Breast imaging reporting and data system: ACR BI-RADS -Breast imaging Atlas, 4th Edition. Reston, VA; American College of Radiology.

2. Sickles EA. Breast calcifications: mammographic evaluation. Radiology 1986; 160(2):289-293.

3. Boyd N, Guo H, Martin L, Sun L, Stone J, Fishell E, Jong R, Hislop G, Chiarelli A, Minkin S, Yaffe M. Mammographic density and the risk and detection of breast cancer. N Engl J Med 2007; 356(3):227-236.

4. Chen J, Silver D, Cantor S, Livingston D, Scully R. *BRCA1*, *BRCA2*, and Rad51 operate in a common DNA damage response pathway. Cancer Res 1999; 59(7 suppl):1752s-1756s.

5. Law J, Faulkner K. Cancers detected and induced, and associated risk and benefit, in a breast screening programme. BR J Radiol 2001; 74(888):1121-1127.

6. Kneeshaw P, Lowry M, Manton D, Hubbard A, Drew J, Turnbull L. Differentiation of benign from malignant breast disease associated with screening detected microcalcifications using dynamic contrast enhanced magnetic resonance imaging. The Breast 2006; 15(1): 29-38.

7. Iacconi C. Diffusion and perfusion of the breast. Eur J Radiol 2010; 76(3):386-390.

8.   Valdes Hernandez Mdel C, Maconick LC, Tan EM, Wardlaw JM. Identification of mineral deposits in the brain on radiological images: a systematic review. Eur Radiol 2012; 22(11):2371-2381.

9.   Yamada N, Imakita S, Sakuma T, Takamiya M. Intracanial calcification on gradient-echo phase image: depiction of diamagnetic susceptibility. Radiology 1996; 198(1):171-178.

10.   Schenck JF. The role of magnetic susceptibility in magnetic resonance imaging: MRI magnetic compatibility of the first and second kinds. Med Phys 1996; 23(6):815-850.

11.   Mills P, Wu Y, Ho C, Ahrens E. Sensitive and automated detection of iron-oxide-labeled cells using phase image cross-correlation analysis. Magnetic Resonance Imaging 2008; 26:618-628.

12.   Jackson J. 1999. Classical electrodynamics, 3rd Ed. New York:Wiley.

13.   Fatemi-Ardekani A, Boylan C, Noseworthy M. Identification of breast calcification using magnetic resonance imaging. Med Phys 2009; 36(12):5429-5436.

14.   James D, Clymer B, Schmalbrock P. Texture detection of simulated microcalcification susceptibility effects in magnetic resonance imaging of breasts. J Magn Reson Imaging 2001; 13(6):876-881.

15.   Stehouwer B, Leeuw H, Seevinck P, Visser F, Luijten P, Klomp D, van Diest P, Bakker C, Veldhuis W. Detection of breast micro-calcifications at high-field MRI. Proc 20th Mtg ISMRM 2012; Melbourne, Victoria, Australia: Abstract.

16. Haacke M, Xu Y, Cheng Y, Reichenbach J. Susceptibility weighted imaging (SWI). Magn Reson Med 2004; 52(3):612-618.

17. Bakker C, Leeuw H, Vincken K, Vonken E, Hendrikse J. Phase gradient mapping as an aid in the analysis of object-induced and system-related phase perturbations in MRI. Phys Med Biol 2008; 53(18):N349-N358.

18. Lai C, Shaw C, Whitman G, Johnston D, Yang W, Selinko V, Arribas E, Dogan B, Kappadath S. Visibility of simulated microcalcifications – a hardcopy-based comparison of three mammographic systems. Med Phys 2005; 32(1):182-194.

19. Cowen A, Launders J, Jadav M, Brettle D. Visibility of microcalcifications in computed and screen-film mammography. Phys Med Biol 1997; 42(8):1533-1548.

20. Kopans D. 1998. Breast imaging, 2nd Ed. Philadelphia, PA: Lippincott-Raven.

21. Krug R, Larson P, Wang C, Burghardt A, Kelley D, Link T, Zhang X, Vigneron D, Mujumdar S. Ultrashort echo time MRI of cortical cone at 7 Tesla field strength: a feasiblity study. J Magn Reson Imaging 2011; 34(3):691-695.

22. Brown R, Megorty K, Moy L, DeGregorio S, Sodickson D, Wiggins G. Sub-millimeter breast imaging and relaxivity characterization at 7T. Proc 19th Mtg ISMRM 2011; Montreal, Quebec, Canada: Abstract.

23. Porter DJ. Non-invasive MRI thermometry with PRF method: study of susceptibility effects. Magn Res Med 1995; 34(3):359-367.

24. Bhagwandien R, Moerland MA, Bakker CJC, Beersma R, Lagendijk JJ. Numerical analysis of the magnetic field for arbitrary magnetic susceptibility distributions in 3D. Magn Reson Imaging. 1994; 12(1)101-107.

25. Balac S. Caloz G, Cathelineau G, Chauvel B, de Certaines JD. Integral method for numerical simulation of MRI artifacts induced by metallic implants. Magn Reson Med 2001; 45(4);724-727.

26. Salomir R, De Senneville B, Moonen C. A fast calculation method for magnetic field inhomogeneity due to an arbitrary distribution of bulk susceptibility. Concept Magn Reson B 2003; 19B(1):26-34.

27. Hoffman RE. Measurement of magnetic susceptibility and calculation of shape factor of NMR samples. J Magn Reson Imaging 2006; 178(2):237-247.

28. Wang Y, Yu Y, Li D, Bae KT. Artery and vein separation using susceptibility-dependent phase in contrast-enhanced MRA. J Magn Reson Imaging 2000; 12:661–670.

29. Li R. Automatic placement of regions of interest in medical images using image registration. MSEE Thesis. 2001; Vanderbilt University.

30. Hoffman R E. Quantification of glands and fat in breast tissue: An experimental determination. Ann Anat 2002; 184(2):181-184.

31. Shellock F G. Reference manual for magnetic resonance safety, implants, and devices, 2005 Edition. Los Angeles, CA: Biomedical Research Publishing Group.

32. Klomp DW, van de Bank BL, Raaijmakers A, Korteweg MA, Possanzini C, Boer VO, van de Berg CA, van de Bosch MA, Luijten PR. 31P MRSI and 1H MRS at 7T: initial results in human breast cancer. NMR Biomed 2011; 24(10):1337-1342.

33. Korteweg MA, Veldhuis WB, Visser F, Luijten PR, Mali WP, van Diest PJ, van den Bosch MA, Klomp DJ. Feasibility of 7 Tesla breast magnetic resonance imaging determination of intrinsic sensitivity and high-resolution magnetic resonance imaging, diffusion-weighted imaging, and (1)H-magnetic resonance spectroscopy of breast cancer patients receiving neoadjuvant therapy. Invest Radiol 2011; 46(6):370-376.

34. Lustig M, Donoho DL, Pauly JM. Sparse MRI: the application compressed sensing for rapid MR imaging. Mag Reson Med 2007; 58(6):1182-95.

35. Hosmer DW, Lemeshow S, Sturdivant R. 2013. Applied logistic regression, 3rd Ed. New York:Wiley.